



1 **The Usumacinta-Grijalva beach-ridge plain in southern Mexico:**
2 **a high-resolution archive of river discharge and precipitation**

3
4 Kees Nooren¹, Wim Z. Hoek¹, Tim Winkels¹, Annika Huizinga¹, Hans van der Plicht^{2,3}, Remke
5 L. van Dam^{4,5,6}, Sytze van Heteren⁷, Manfred J. van Bergen¹, Maarten A. Prins⁸, Tony Reimann⁹,
6 Jakob Wallinga⁹, Kim M. Cohen^{1,7,10}, Philip Minderhoud¹ and Hans Middelkoop¹

7
8 ¹Utrecht University, Faculty of Geosciences, 3508 TC Utrecht, The Netherlands;

9 ²Groningen University, Center for Isotope Research, 9747 AG Groningen, The Netherlands;

10 ³Leiden University, Faculty of Archaeology, 2333 CC Leiden, The Netherlands

11 ⁴Centro Federal de Educação Tecnológica de Minas Gerais, Department of Civil Engineering
12 (CEFET-MG), CEP 30510-000, Belo Horizonte, Brazil

13 ⁵Michigan State University, Department of Earth and Environmental Sciences, East Lansing, MI
14 48824, United States

15 ⁶Queensland University of Technology, Science and Engineering Faculty, Institute for Future
16 Environments, Brisbane, QLD 4001, Australia

17 ⁷TNO – Geological Survey of the Netherlands, Geomodeling Department, 3508 TA Utrecht, The
18 Netherlands

19 ⁸Vrije Universiteit, Faculty of Earth and Life Sciences, 1081 HV Amsterdam, the Netherlands

20 ⁹Wageningen University, Soil Geography and Landscape Group & Netherlands Centre for
21 Luminescence dating, 6708 PB Wageningen, The Netherlands

22 ¹⁰Deltares, Department of Applied Geology and Geophysics, 3584 CB Utrecht, The Netherlands.

23
24 *Correspondence to:* Kees Nooren (c.a.m.nooren@uu.nl)

25
26 **Abstract**

27
28 The beach-ridge sequence of the Usumacinta-Grijalva delta borders a 300-km-long section of the
29 Southern Mexico Gulf coast. With around 500 beach ridges formed in the last 6500 years, the
30 sequence is unsurpassed in the world in terms of numbers of individual ridges preserved,
31 continuity of the record, and temporal resolution. We mapped and dated the most extensively
32 accreted part of the sequence, linking six phases of accretion to river-mouth reconfigurations and
33 constraining their ages with ¹⁴C and OSL dating. The geomorphological and sedimentological
34 reconstruction relied on LiDAR data, coring transects, GPR measurements, grain-size analyses
35 and chemical fingerprinting of volcanic glass and pumice encountered within the beach and dune
36 deposits.

37 We demonstrate that the beach-ridge complex was formed under ample long-term fluvial
38 sediment supply and shorter-term wave- and aeolian modulated sediment reworking. The
39 abundance of fluvially supplied sand is explained by the presence of easily weatherable Los
40 Chocoyos ignimbrites from the ca. 84 ka eruption of Atitlán volcano (Guatemala) in the
41 catchment of the Usumacinta River. Autocyclic processes seem responsible for the formation of
42 ridge/swale couplets. Fluctuations in their periodicity (ranging from 6-19 yrs) are governed by
43 progradation rate, and are therefore not indicative of sea level fluctuations or variability in storm
44 activity. The fine sandy beach ridges are mainly swash built. Ridge elevation, however, is
45 strongly influenced by aeolian accretion during the time the ridge is located next to the beach.
46 Beach-ridge elevation is negatively correlated with progradation rate, which we relate to the
47 variability in sediment supply to the coastal zone, reflecting decadal-scale precipitation changes
48 within the river catchment. In the Southern Mexican delta plain, the coastal beach ridges
49 therefore appear to be excellent recorders of hinterland precipitation.

50



51 **1 Introduction**

52

53 Beach-ridge plains with long sequences holding many individual ridges consisting of coral
54 rubble, shell hash, cobbles, gravel and/or sand are widely distributed across the globe. They have
55 developed along marine and lakeshores under favourable wind and wave conditions, and
56 sufficient long-term sediment supply.

57

58 During the past few decades, research on beach-ridge sequences has progressed from describing
59 their morphology and possible origins (Taylor and Stone, 1996; Otvos, 2000) to enabling their
60 usage for palaeoenvironmental reconstructions. They can be used to assess external controls of
61 (relative) sea-level rise, land subsidence, variations in storm impact, and changes in climate and
62 upstream land use (Scheffers et al., 2012; Tamura, 2012 and references therein). They also may
63 include markers left by catastrophic events like volcanic eruptions (Nieuwenhuys and
64 Kroonenberg, 1994; Nooren et al., 2017), and host soils that are suitable for chronosequence
65 studies (Nielsen et al., 2010; May et al., 2015; Hinojosa et al., 2016).

66

67 The number of preserved ridges determines the extent of the palaeo-environmental record stored
68 in the associated sediments, with resolutions up to decadal scale (cf. Curray et al., 1969; Nielsen
69 et al., 2006; Milana et al., in press). The largest beach-ridge plains with multiple parallel beach
70 ridges are formed along medium- to low-energy shorelines of lakes and seas. The beach-ridge
71 plain on the seaward margin of the terrestrial Usumacinta-Grijalva delta in southern Mexico (Fig.
72 1a) is probably the world's largest. Since the strong reduction in the rate of postglacial sea-level
73 rise in the mid-Holocene, hundreds of semi-parallel sandy beach ridges formed across a shore-
74 perpendicular distance of more than 20 km. In our study area near Frontera (Fig. 1b) beach
75 ridges include aeolian topsets composed of backshore-fringing foredunes. In this paper, we use
76 Otvos's (2000) broad definition of beach ridges, including all 'relict, semi-parallel, multiple
77 ridges' formed by waves (berm ridges), wind (multiple ridges originating as foredunes) or a
78 combination of both.

79

80 Earlier morphological studies (Psuty, 1965, 1967; West et al., 1969) identified three main phases
81 in the development of the beach-ridge plain, each linked to a specific position of the rivers' main
82 channels (Fig. 1b). The north-easterly branches of the Grijalva fan-delta river system created
83 favourable conditions for local beach-ridge-complex initiation and development during Phase 1,
84 the Usumacinta (with the San Pablo y San Pedro River (SP y SP in Fig. 1b as the main outlet)
85 during Phase 2 and both rivers (though a combined outlet near Frontera) during Phase 3. Psuty
86 (1965, 1967) proposed an important role to storm surges and overwash in the formation of the
87 beach ridges. Aguayo et al. (1999) established a preliminary chronology of beach-ridge
88 formation on the basis of radiocarbon-dated bivalves and gastropods. Our study elaborates on
89 these pioneering works, aiming to establish a robust chronology for the beach-ridge sequence
90 and to understand the apparent periodical variations in beach-ridge height that are seen in LiDAR
91 imagery of the study area (Fig. 2a).

92

93 In the long-term (10^3 years), the considerable accretion of the beach ridge complex has been
94 driven by steady sediment supply by the Usumacinta and Grijalva Rivers (West et al., 1969).
95 Much of this sediment has been generated in their upper catchments and routed through the delta
96 plain to the coastal zone. Morphometric variations between the main phases of beach-ridge
97 formation (Fig. 1b) is mainly influenced by spatiotemporal variability in the positions of the river
98 mouths, size of the feeding river and magnitude of sediment fluxes carried by the water. Studies
99 on other beach-ridge systems suggest that shorter term (10^1 - 10^2 years) variability can reflect
100 oscillations in river-mouth sediment supply (Brooke et al., 2008a; Tamura, 2012), potentially



101 making the Usumacinta-Grijalva beach-ridge sequence a proxy record for variability in
102 precipitation in the hinterland.

103
104 To test this hypothesis, we conducted a detailed geomorphological and sedimentological field
105 study, linking LiDAR data to cored and geophysically surveyed transects, and extensive
106 sediment analyses and dating. Our study covers 150 km of the beach-ridge complex in a shore-
107 parallel direction and 20 km in a shore-normal direction. Grain-size and mineralogical analyses
108 are potentially powerful tools to understand transport and deposition mechanisms of beach-ridge
109 sands (cf. Visher, 1969), but have scarcely been applied in recent beach-ridge studies (exceptions
110 are Guedes et al., 2011; Garrison et al., 2012). Volcanic glass and pumice fragments are highly
111 informative components of the beach-ridge sands (Nooren et al., 2017), and have been
112 chemically fingerprinted to determine their provenance. The internal architecture of the beach
113 ridges was imaged with ground-penetrating radar (GPR), as in other beach-ridge and coastal-
114 barrier studies (e.g. Jol et al., 1996; Van Heteren, 1998; Bristow and Pucillo, 2006; Forrest,
115 2007; Oliver, 2016).

116
117 A detailed chronology of the sequence was established from the combined deployment of
118 Optically Stimulated Luminescence (OSL) on quartz grains (quartz content of the sand is 50 to
119 65%, Aguayo et al., 1999), and AMS ^{14}C dating of thin layers of terrestrial organic debris (leaf
120 fragments) in the beach-ridge sand. Here we expand on the chronology of a 3-km-long beach-
121 ridge subsection documented in Nooren et al. (2017). Quartz-grain OSL dating has been widely
122 used for establishing the age of coastal deposits in general (e.g. Ballarini et al., 2003; Nielsen et
123 al., 2006; Reimann et al., 2011) and beach-ridge sequences in particular (Tamura, 2012 and
124 references therein; Oliver et al., 2015; Rémillard et al., 2015; Vespremeanu-Stroe et al., 2016;
125 Milana et al., in press), but its combination with AMS ^{14}C dating of thin organic debris layers is
126 presented here for the first time. It provides a unique opportunity for cross-validating the
127 methods.

128
129

130 **2 Geographical Setting**

131

132 The study area is part of the beach-ridge system along the edge of the Holocene Usumacinta-
133 Grijalva delta plain, and stretches from Paraiso in the west to Ciudad del Carmen in the east (Fig.
134 1b). The delta plain and its hinterland have a humid tropical climate with mean annual
135 precipitation ranging from 1000 to 1500 mm in the highlands of the Chiapas Massif and along
136 the Tabasco coast to locally more than 5000 mm in the mountain foothills in between (West et
137 al., 1969; Hijmans et al., 2005). Approximately 80 % of the annual precipitation falls in a rainy
138 season that lasts from June until November. The excess or effective precipitation contributing to
139 river discharge is around 40-60 % (Table 1). Peak discharges are related to the passage of large
140 tropical depressions, most frequently occurring in September and October.

141

142 The drainage basin of the Usumacinta River is dominated by a Cretaceous limestone plateau,
143 folded during the Paleogene (Padilla and Sanchez, 2007), with elevations rarely exceeding 700 m
144 above mean sea level (m+MSL). The headwater catchments of this river, however, are composed
145 of pre-Mesozoic plutonic, metamorphic and volcanic rocks (Fig. 1a). These uplands are dotted
146 with large remnants of Los Chocoyos ignimbrites left by a Pleistocene caldera-forming eruption
147 at Atilán volcanic centre in southern Guatemala. The Los Chocoyos ignimbrites are also found
148 in the upper drainage basin of the Grijalva River, up to 130 km from the Atilán caldera
149 (Sánchez-Núñez et al., 2015), but they do not have the same extent as the deposits within the
150 Usumacinta drainage basin.



151

152 Presently, routing of sediment from upstream to downstream reaches of the Usumacinta River is
153 blocked by the Chixoy hydroelectric dam at Pueblo Viejo (Fig. 1a). This man-made obstacle has
154 reduced sediment transport to the coast since its completion in 1983. High erosion rates have
155 caused rapid infill of the reservoir behind the dam. Between 1983 and 2009, approximately
156 $158 \cdot 10^6 \text{ m}^3$ of sediment has accumulated at an average rate of $6.1 \cdot 10^6 \text{ m}^3/\text{year}$ (Jom Morán,
157 2010). The total volume of upland source material and the rate at which it is transported
158 downriver show that the Usumacinta could have contributed a sufficient amount of sediment for
159 the rapid progradation of the beach-ridge plain. Nieuwenhuysen and Kroonenberg (1994)
160 demonstrated a similar important role of volcanoclastic sediments in the formation of Holocene
161 beach ridges in Costa Rica.

162

163 The coastal zone experiences a diurnal tide with a microtidal range between 0.25 and 0.75 m.
164 During most of the year, low-energy waves coming from the northeast with swells of 0.3 to 0.7
165 m produce a wave-generated longshore current carrying river sediments westwards (West et al.,
166 1969). Under these fair-weather conditions, beach accretion is common (Psuty, 1965, 1967),
167 building out the promontories of active river mouths. Usually some 20 to 25 ‘Nortes’ or frontal
168 storms hit the area between October and March. These produce strong north-westerly winds
169 generating swells of 1.2 to 1.7 m as well as local longshore-current reversals and commensurate
170 beach erosion (West et al., 1969). Wave climate increases westward in the dominant longshore-
171 current direction, a result of relatively steeper shoreface slopes in the western part of the study
172 area (notice 10-m depth contour in Fig. 1b). Newly formed beach ridges are rapidly colonised
173 and stabilised by vegetation, most noticeably and dominantly by *Ipomoea pes-caprae*, a salt-
174 tolerant coastal pioneer species (Castillo et al., 1991; Gallego-Fernández and Martínez, 2011).

175

176

177 3 Materials and Methods

178

179 3.1 Geomorphological and sedimentological survey

180 The LiDAR data (Fig. 2a) were originally acquired in April-May 2008 and processed by
181 Mexico’s National Institute of Statistics and Geography (INEGI). The derived DEM product has
182 a cell size of 5x5 m, has cm-scale vertical resolution and is accurate to 0.15-0.30 m (Ramos et
183 al., 2009). The LiDAR imagery is used to morphometrically distinguish main and sub-phases of
184 progradational beach-ridge formation, focusing on internal similarity in ridge dimensions,
185 orientation, and lateral and cross-cutting relationships with river-channel morphology. We
186 identified and defined sub-phases that correspond to periods of relatively stable river-mouth
187 configurations, with smaller and larger river-network reconfigurations as the breaks between.
188 Avulsions affecting the main river branches have drastically changed their position in several
189 instances, and, consequently, the supply of sediment to the beach-ridge system. This changing
190 supply is particularly recognisable from the truncation of beach ridges of former river
191 promontories at the modern coastline, but can also be seen from orientation shifts in beach-ridge
192 alignments within the beach-ridge complex.

193

194 LiDAR-inferred morphometric phases were ground-truthed using sediment composition and
195 chronometric results from four field campaigns in the period 2011-2015. To describe and sample
196 the sandy, waterlogged lithology, sediment cores reaching 4 to 11 m depth were taken with a soil
197 auger and a Van der Staay suction corer (Van de Meene et al., 1979). Boreholes were placed
198 along three shore-normal (A, B and C) and two shore-parallel (D1 (youngest beach ridge) and
199 D2) transects (Fig. 2a). To support the interpretation of the grain-size data, surficial nearshore



200 sediments were sampled off Playa La Estrella in April 2013 for modern-analogue study of the
201 shore-normal sorting processes.

202

203 The shore-parallel transects aimed at characterising the aeolian facies encountered on the most
204 recent beach ridge, and the swash facies encountered at ~1 m below MSL in a relatively elevated
205 fossil beach ridge. The shore-normal transects aimed at establishing the progradational
206 chronology and its relation with river shifts, with densest sampling along Transects A and B
207 (Fig. 2b). A 3-km-long subsection of Transect A, containing evidence for a volcanic eruption of
208 El Chichón in 540 CE, was studied in substantial detail (Nooren et al., 2017). For consistency,
209 each coring location was chosen at the seaward foot of an individual ridge, except when the
210 aeolian cap on top of the ridges was sampled. Bagged samples of sand were collected at 0.2-0.5
211 m core-intervals. Encountered organic debris-rich layers were sampled and stored in a cold room
212 (4°C) pending further processing for AMS ¹⁴C dating. For OSL dating, nineteen samples were
213 collected in 30-cm-long opaque tubes from the bottom of shallow hand-augered boreholes during
214 the dry seasons of 2012 and 2013. OSL sample 450 was collected from a soil pit dug in a beach
215 ridge for use in a chronosequence study (Hinojosa et al., 2016).

216

217 More than one thousand sand samples were collected in the field, transported to the Netherlands,
218 dried at 105 °C, and stored at room temperature. Magnetic susceptibility was measured on all
219 dried sand samples with a hand-held ZH Instruments SM 30. Calcium carbonate was measured
220 on sand samples from the two shore-parallel transects and on sand samples from cores 192, 252,
221 432, 433, 435, 452 and 453 (Fig. 3), to estimate the maximum depths of pedogenic
222 decalcification, which indicates the position of the phreatic surface (ground water level and, by
223 proxy MSL). Calcium carbonate was measured with a Scheibler Calcimeter, by adding 10% HCl
224 solution to 1 g sediment and measuring the produced CO₂ volumetrically. Carbonate content is
225 expressed as weight percentage CaCO₃. Grain-size analyses (range 0.15 – 2000 μm) were
226 conducted with a Sympatec HELOS/KR laser diffraction particle sizer, equipped with an
227 advanced wet disperser (QIXEL). Before measurements, organic matter and carbonates were
228 removed with 20% H₂O₂ and 10% HCl. Grain-size parameters (median, sorting, skewness and
229 kurtosis) were calculated following Folk and Ward (1957).

230

231 Grain-size and magnetic-susceptibility investigations were supported by a limited number of
232 heavy-mineral analyses to characterise the source material. Heavy minerals were separated with
233 a heavy-liquid solution (Sodium Polytungstate, Na₆[H₂W₁₂O₄₀]) with a density of 2.85g/cm³, and
234 identified under a polarised-light microscope. Volcanic glass shards and a pumice clast retrieved
235 from four beach-ridge cores along Transect A, covering a large temporal range in beach-ridge
236 formation (Fig. 2b and 3a, samples 336, 252, 193 and 197), were chemically fingerprinted to
237 identify the eruption source(s). Major-element compositions of the glass shards were determined
238 on 5-12 particles per sample with a Jeol JXA 8600 microprobe equipped with five wavelength-
239 dispersive spectrometers. Measurements were performed by WDS using 15kV acceleration
240 voltage, 10nA beam current and a defocused beam (5μm spot size) to minimise mobilisation of
241 sodium. Instrumental performance and calibration were monitored by repeated analyses of
242 natural glass standards (rhyolitic USNM 72854 VG-568 and basaltic USNM 111240 VG-2) and
243 in-house mineral standards.

244

245 **3.2 AMS radiocarbon and OSL dating**

246 Within the beach ridges, 1- to 5-cm-thick layers of organic debris were commonly found,
247 especially at locations relatively close to a (former) river mouth (Transects A and B3). The layers
248 contained charcoal, wood and leaf fragments, often mixed with shell fragments. This organic
249 material is transported to the coast by the rivers, then further distributed by longshore currents to



250 eventually be incorporated into the beach ridge facies. The debris is a mixture of apparently
251 younger (hardly harmed) and older (rounded edges) reworked material. Reworking was
252 especially evident from the commonly rounded edges of wood and charcoal fragments in the
253 detritus cocktail. Reworked organic material was purposely avoided in our sampling (apart from
254 test samples to demonstrate the associated danger of age overestimation) and age-distance
255 modelling.

256
257 Thirty-five terrestrial macro-remains (mainly leaf fragments), isolated from organic debris
258 layers, were standard AAA pretreated, and ^{14}C dated using an AMS facility (Van der Plicht et al.,
259 2000). Ages were reported in yr BP, using the Libby half-life and corrected for isotopic
260 fractionation via $\delta^{13}\text{C}$ (Mook and Van der Plicht, 1999). They were calibrated with the software
261 package OxCal 4.2 (Bronk Ramsey, 2009) using the IntCal13 calibration curve (Reimer et al.,
262 2013).

263
264 Twenty OSL samples were dated using Risø TL/OSL DA15/20 readers (Bøtter-Jensen et al.,
265 2003), equipped with Sr/Y beta sources. About 130 g material from the (light-exposed) outer
266 parts of the sample tubes was used for dose-rate determination. High-resolution gamma
267 spectrometry was used to determine radionuclide-activity concentrations (^{40}K , and several
268 nuclides from the U and Th decay chains). Measured values were converted to environmental
269 dose rates using conversion factors of Guerin et al. (2011), assuming immediate burial of the
270 samples to present depth, and accounting for attenuation due to water and organic material
271 (Aitken, 1998) and cosmic-ray contributions (Prescott and Hutton, 1994). For OSL samples
272 obtained from below the groundwater table, a water content of $25 \pm 5\%$ by weight was used
273 (pore space fully water saturated), assuming permanent saturation over the entire burial period.
274 For some of the older samples, it is likely that they were deposited above contemporary
275 groundwater levels (Fig. 3b). However, at this stage it is not possible to make a more realistic
276 estimation of the average water content over the entire burial period. Dependency of dose rates
277 and hence OSL ages on water content, implies that OSL age estimates will decrease by
278 approximately 1 % for each weight % decrease in water content (Aitken, 1998). For two OSL
279 samples taken above the groundwater table, a water content of $5 \pm 3\%$ was used (moisture
280 contents at field capacity).

281
282 OSL samples were prepared following standard procedures including sieving and chemical
283 treatment with H_2O_2 , HCl and HF, to yield sand-sized purified quartz of 212–250 μm . For
284 aeolian sample 179, the fraction 180–212 μm was used. Quartz OSL signals were detected
285 through a 7.5 mm Hoya U340 filter, and an early background approach was applied to obtain a
286 net signal that is dominated by the fast OSL component of quartz (Cunningham and Wallinga,
287 2010). The OSL IR depletion ratio of Duller (2003) was used to check for feldspar
288 contamination. Equivalent doses were determined on small aliquots (2 mm, ~60 grains) using the
289 Single Aliquot Regenerative dose procedure (Murray and Wintle, 2003). The Central Age Model
290 (CAM, Galbraith et al. 1999) was used to determine over-dispersion in the resulting equivalent-
291 dose distributions (i.e. spread in results on individual aliquots that is not explained by the
292 analytical uncertainties) and for burial-dose estimation. In case of high over-dispersion (>30%)
293 in combination with skewed dose distribution, the burial dose was estimated using a
294 bootstrapped version of the Minimum Age Model (Cunningham and Wallinga, 2012). OSL ages
295 are determined by dividing the sample burial dose by the sample dose rate and reported in Year
296 CE, with 1-sigma uncertainty ranges. For each sample, validity of the OSL age was assessed on
297 the basis of the equivalent-dose distribution.

298



299 The full set of calibrated AMS ^{14}C and OSL ages was used to establish an age-distance model,
300 using the P_sequence module of the Oxcal 4.2 programme (Bronk Ramsey, 2009; 2016). We
301 furthermore demonstrate the variability in age-distance models for part of Transect B if we
302 assume a constant aeolian accretion rate, following the approach of Minderhoud et al. (2016).
303

304 **3.3 Ground-penetrating radar**

305 GPR surveys were conducted at the end of the dry season in June 2012 along parts of the
306 transects (Fig. 2a). Data were collected using a MALA ProEx system with 250-MHz shielded
307 antennas and an odometer wheel for accurate positioning (0.1 m step size). For the time-depth
308 conversion, we used signal velocities of 0.125 (based on the move-out of diffraction hyperbolas)
309 and 0.06 m/ns for deposits above and below the groundwater table, respectively.
310

311 **3.4 Beach-ridge elevation and accretion volumes**

312 Fifteen cross-normal ribbon-shaped elevation transects (Fig. 2b) were sampled from the LiDAR
313 based DEM, and combined with the dating information to calculate the temporal variability in
314 beach-ridge elevation and accretion volumes. To exclude short-term variability in beach-ridge
315 elevation and to minimise the effect of local erroneous elevation values we divided the 1-km-
316 wide ribbons into multiple polygons (Fig. 2b). Each polygon included at least one, but on
317 average a few ridge/swale couplets.
318

319 We estimated an average thickness for the Holocene beach-ridge deposits of 10 ± 2 m, based on
320 geophysical tests conducted near the current combined Usumacinta-Grijalva River outlet
321 (Administración Portuaria Integral de Dos Bocas S.A. de C.V., 2005). Unfortunately, we have
322 limited information regarding the inland spatial variability in thickness of the beach ridge
323 complex, and our deepest Van der Staay core of 11 m (core 426, Figs. 3a and 4) did not penetrate
324 the base of the Holocene beach-ridge deposits at this location.
325

326 Aeolian accretion sub-volumes were calculated from the ribbon-averaged estimated mean beach-
327 ridge elevation. The calculation assumed all sandy deposits above an estimated average swash
328 run-up height of 0.5 m above MSL at the time of beach-ridge formation to be aeolian in origin.
329 We used our decalcification depth observations (which sits decimetres deeper than the current
330 groundwater level at more inland beach ridges) and the resemblance of this signal with Gischler
331 and Hudson's (2004) sea-level curve for Belize, to assess the MSL positions at the time of
332 beach-ridge formation. The calculations were performed for Phase 2 and Phase 3. Along
333 Transect A we added 1 m to the raw LiDAR DEM values because the surface elevations as
334 estimated during the fieldwork period were systematically 1 m higher than the first-generation
335 DEM product for this subarea. We assume that the groundwater level by the end of the dry
336 season in 2012 and 2013 should at least correspond to or be above present MSL, as was the case
337 at core locations along Transects B and C.
338

339 **4 Results**

340 **4.1 LiDAR DEM analyses**

341 The three main phases in beach-ridge formation (Psuty, 1965, 1967; West et al., 1969) are easily
342 discernible from the LiDAR-based DEM (Fig. 2a). Approximately 500 beach ridges can be
343 distinguished. Their spacing is typically between 20-100 m, and mean surface elevations along
344 the three shore-normal transects vary between 0.5 and 3.5 m+MSL (Fig. 3). Beach ridges are
345 relative low and widely spaced near (former) river mouths. Away from a river mouth they merge
346 or become more closely spaced. Beach-ridge elevation, however, tends to increase with distance
347
348



349 from a river mouth. The most elevated beach ridges (up to 5 m+MSL) are found in the western
350 part of the study area (Fig. 2a) – on the downdrift side of the system. The influence of drift
351 direction is also apparent in the modest asymmetry of the truncated Phase 2 promontory at the
352 mouth of the SP y SP River and in the strong westward deflection of the mouth of the Gonzalez
353 River (Fig. 2b).

354 Two faults (Fig. 2b), almost perpendicular to the orientation of the beach ridges, may be
355 responsible for the slight east-west tilt of ridges in this part of the study area. The DEM shows no
356 evidence for any significant horizontal displacement along NW-SE oriented strike-slip faults
357 described by Aguayo et al. (1999).

358 Scour holes, possible features produced by large storm surges, are clearly identifiable along only
359 one beach ridge in the western part of the study area (Fig. 2b), and washovers are not apparent
360 from the DEM, indicating that few extreme storm events left clear traces in the area.

361

362 **4.2 Beach-ridge chronology**

363 The 35 AMS ^{14}C and 20 OSL sample ages (Figs. 2b, 3 and 4, Tables A1 and A2) offer a
364 significant refinement of the preliminary beach-ridge chronology proposed by Aguayo et al.
365 (1999) on the basis of radiocarbon-dated shell material. The resolution offered by the large
366 number of dated samples facilitated the development of age-distance models for the progradation
367 of the beach-ridge plain (Figs. 3 and 4), used in turn to reconstruct the palaeoshorelines as
368 indicated in Figure 5a.

369

370 The sequence of calibrated ^{14}C ages shows very good internal consistency, with only two
371 statistically significant age reversals (both in Transect A2; Fig. 4c). This more than fair
372 agreement of ^{14}C ages with vertical stratigraphic order and lateral geographic position gives
373 confidence to their representativeness for deposition age. Nevertheless, dated organic detrital
374 fragments give '*Terminus Ante Quem*' ages that may be older than the beach-ridge sand in which
375 they were entrained. Charcoal fragments have been found to be many hundreds of years older
376 than the more fragile leaf fragments from the same debris layer (Fig. 3a and Table A1, sample
377 252 and 336), and do not provide a reliable age of final deposition. We therefore avoided wood
378 and charcoal in our sample analysis and only used dated leaf fragments for the age-distance
379 models (Fig. 3). Of all the terrestrial macro-remains in the organic debris layers, fragile leaves
380 are assumed to be the least likely to have survived repeated reworking. There are some
381 indications, however, that even the leaf fragments have undergone some reworking, because
382 samples taken farther from the former river mouth in Transect B2, appear to be 200-500 years
383 older than the LiDAR-tracing projected AMS ^{14}C ages of samples taken closer to the river mouth
384 in Transect A (Figs. 3b and B1).

385

386 Quartz OSL behaviour of the samples showed suitability for dating. A dose-recovery experiment
387 indicated that a given dose could be retrieved accurately (dose-recovery ratio 0.997 ± 0.014 ,
388 $n=39$). Equivalent-dose distributions were normally distributed and showed over-dispersion as
389 expected for well-bleached deposits (average 18%, $n=17$). For three samples (179, 427 and 444),
390 higher over-dispersion ($>30\%$) was observed. The reliability of samples 179 and 427 was
391 considered questionable because the equivalent-dose distributions lacked the characteristic
392 skewness that would characterise over-dispersion due to heterogeneous bleaching (e.g. Wallinga,
393 2002). For sample 444, heterogeneous bleaching was inferred from the large over-dispersion in
394 combination with positive skewness in the equivalent-dose distribution. For this sample a burial
395 dose was determined using a bootstrapped version of the Minimum Age Model (Cunningham
396 and Wallinga, 2012), resulting in a higher-confidence OSL age.

397



398 Dose rates were found to vary between 1.83 ± 0.08 and 2.66 ± 0.10 Gy/ka (mean 2.18 Gy/ka).
399 These values are lower than those reported for Usumacinta levee deposits (2.38 – 4.55 Gy/ka,
400 Muñoz-Salinas et al., 2016). The difference is likely related to lower amounts of silt and clay in
401 the beach ridges than in the levees. Dose rates are much higher than the extremely low values
402 reported for the quartz-rich beach ridges in Florida (e.g. Otvos, 2005; López and Rink, 2008;
403 Rink and López, 2010).

404
405 Quartz OSL ages are internally highly consistent, and agree well with the calibrated ^{14}C ages
406 (Figs. 3 and 4), underscoring the usefulness of OSL dating in the establishment of beach-ridge
407 chronologies (cf. Tamura, 2012).

408
409 For two samples (451 and 450), collected at the same location but at different depths, OSL
410 results suggested an age difference of about 600 years. A possible partial explanation is that the
411 water-content estimations for these samples (field capacity for OSL sample 451; water-saturated
412 for sample 450) (Table A2) are not correct. If more similar water contents are assumed for both
413 samples, the age difference is much reduced, highlighting the importance of water-content
414 estimation in OSL dating. An alternative, or additional, explanation could be that the sediment
415 above the groundwater table was reworked (e.g. through bioturbation). The spread in equivalent-
416 dose distribution for sample 179 may indicate such reworking, but for sample 451 the
417 equivalent-dose distribution provides no evidence of reworking. For the age-distance model, we
418 excluded OSL ages that were judged to be of questionable validity (179 and 427) and those
419 obtained from sediments above the groundwater table (179 and 451).

420
421 The age-distance models for Transects A and B are presented in Fig. 3. For a 3-km section
422 (Transect A2), the age-distance model was published by Nooren et al. (2017; Fig. 4c). Three new
423 OSL analyses (this paper; Table A2 and Fig. 4c), one providing a questionable age (sample 427),
424 corroborate the robustness of that study. Radiocarbon ages of shells reported by Aguayo et al.
425 (1999) do not provide additional age constraints, owing to limitations in accuracy of the shell
426 ages caused by carbon reservoir effects and taphonomic depositional uncertainty.

427
428 We ran a P_{sequence} Bayesian calibration model ($k=0.05 \text{ m}^{-1}$) (Bronk Ramsey, 2009), fed with
429 the AMS ^{14}C and OSL dates and relative shore-normal positions, and with boundaries (i.e.
430 discontinuities) prescribed at the transitions between the three main beach-ridge-formation
431 phases. For the age-distance model of Transect B (Fig. 3b), we projected AMS ^{14}C and OSL ages
432 of samples from Transect A, correlating along the beach-ridge traces in the LiDAR data. Because
433 of the assumed time lag between the final burial of leaf fragments in the beach ridges at smaller
434 (Transect A) and greater (Transect B) distance to the river mouth during Phase 2, in the
435 corresponding part of Transect B the ^{14}C ages of samples 185 and 438 (Fig. 3b) were excluded
436 from the model. We identified one OSL age (sample 437) as an outlier (too old compared to ages
437 of neighbouring samples) and excluded it from the age-distance modelling (Fig. 3b).

438
439 The age-distance model for Transect A (Fig. 3a) shows a long-term average progradation rate
440 that decreased from 4.1 to 3.4 m/y between the start of Phase 2 (~1800 BCE) until the transition
441 between Phases 3A and 3B, dated at ~1050 CE. Progradation rates returned to higher values
442 during Phases 3B and 3C, 4.0 and 4.5 m/y respectively, related to the reconfiguration of the river
443 system and the avulsion of the Usumacinta River around 1050 CE (discussed in section 5.1).

444
445 The age-distance model for Transect B (Fig. 3b) includes a preliminary model for Phase 1 (4500
446 –1800 BCE). The model is based on relatively few samples, including OSL ages sensitive to
447 uncertainty related to water-content assumptions, and must therefore be treated with caution. The



448 age-distance model for Phase 2 has an age range between 1775 ± 95 BCE and 30 ± 95 CE (at
449 1σ), which covers a slightly shorter time period than at Transect A where Phase 2 runs until
450 approximately 150 CE. The LiDAR image shows clear signs of truncated beach ridges between
451 Phases 2 and 3 at Transect B, explaining the occurrence of a hiatus. To investigate possible age-
452 distance scenarios for Transect B (Phase 2), we calculated five possible short- and long-range
453 scenarios (Transect B2-1 till B2-5 in Fig. 2b) by including aeolian accretion (see section 4.6) as a
454 proxy for progradation rate of the beach-ridge plain. The depicted scenarios (Appendix B, Fig.
455 B1) assume shore-normal aeolian accretion activity to be constant between 1800 BCE and 30
456 CE. Under this assumption the most noticeable change in progradation rate occurred around
457 1000 BCE, during a period when relatively high beach ridges are indicative for a strong drop in
458 progradation rate. This is apparent in both long- and short-range scenarios and at all five
459 transects. The long-range scenarios seem to be in better agreement with the mean of the OSL
460 ages. These calculations show the potential to improve age-distance models with additional
461 information regarding the temporal variability in aeolian accretion rates.

462

463 The age-distance model is less reliable for Phase 3A owing to the lack of dated samples along
464 Transect B, the rejection of OSL sample 179 and uncertainties in the projected location of dated
465 samples from Transect A. The age-distance model is very robust again for the period 1050 CE to
466 present (Phases 3B and 3C), with precision of modelled ages in the order of only 10–60 years (at
467 1σ).

468

469 For Transect C the age-distance model (not shown) is preliminary, because it only relies on two
470 AMS ^{14}C dated samples (Table A1), and geomorphological age-projections from Transect A.

471

472 **4.3 Grain-size analyses**

473 The beach ridges consist of moderately well- to well-sorted fine to medium sand. All samples
474 show a unimodal grain-size distribution with a median between 117 and 350 μm (Fig. 5b). The
475 grain-size of sand samples from two shore-parallel transects (Fig. 6) show a general coarsening
476 in the dominant (westward) longshore-transport direction.

477

478 The longshore trend in grain size is apparent in both swash and aeolian facies (Fig. 6), applies
479 along the full length of the study area, and does not appear to be affected by the deltaic
480 promontory of the Usumacinta/Grijalva River in the middle of it. Skewness of the grain-size
481 distribution increases in the dominant longshore-transport direction, denoting an increase in
482 excess fines, and the swash facies tends to get better sorted (decrease in phi values) in the same
483 westward direction. Kurtosis values do not show systematic changes. Magnetic-susceptibility
484 values also tend to increase in a westward direction, with the most elevated values around the
485 (former) waterline, as heavy minerals, including titanomagnetite, preferentially accumulate in the
486 swash zone (Komar, 2007). The high magnetic-susceptibility values for aeolian beach-ridge sand
487 near the mouth of the currently active Usumacinta/Grijalva and Gonzalez Rivers is likely related
488 to the contribution of volcanoclastic material from El Chichón's 1982 eruption, as magnetite
489 enrichment in the beach-ridge sands also occurred after earlier eruptions of El Chichón (Nooren
490 et al., 2017). The CaCO_3 concentration decreases in the longshore transport direction, in line
491 with a decreased influence of calcareous sediment from the calcareous platform in the eastern
492 part of the study area (Ayala-Castanares and Guittierrez-Estrada, 1990) (Fig. 1b).

493

494 The westward increase in median grain size probably relates to an increase in wave energy,
495 which also may have caused the steepening of the shoreface slopes in that same direction. The
496 presence of mega-cusps at beaches near the mouth of the Gonzalez River is an additional
497 indication of relatively strong wave impact on the western side of the system. Similarly, and at



498 first sight contradictory, grain-size coarsening in the longshore-drift direction was observed at
499 Sint George Island (Balsillie, 1995) and along the North Sea beaches of East Anglia, England
500 (McCave, 1978). McCave (1978) explained the coarsening of beach sand in the longshore-
501 transport direction as a result of the winnowing of fines and their offshore transport by tidal
502 currents. Similar processes could be responsible for the westward grain-size coarsening, and
503 could explain the dominance of relatively fine clastic sediments on the continental shelf at the
504 study site (Ayala-Castanares and Guittiérrez-Estrada, 1990) (Fig. 1b). The offshore transport of
505 fines is probably stimulated by the anticyclonic eddy that develops during spring and moves
506 westward along the coast during summer (Salas de León et al., 2008). This eddy influences
507 bottom currents, especially west of Usumacinta/Grijalva River outlet. Lastly, it should be noted
508 that deviations from this general pattern in longshore grain-size distribution do occur. The
509 relatively coarser grain size of the three aeolian samples approximately 10 km west of the SP y
510 SP River for example are probably due to the contribution of eroded and reworked sand from the
511 old promontory of the SP y SP River (Fig. 6).

512

513 Although the major variability in grain-size parameters occurs in a shore-parallel direction,
514 shore-normal sorting processes due to wind and wave activity have resulted in significant
515 variation in grain-size parameters as well (Fig. 7). Surface samples from the modern beach
516 profile at Playa Estrella (Fig. 7a) show an increase in grain size from offshore towards the coast,
517 with coarsest and least-sorted sand occurring in the relatively high-energy swash zone. The
518 grain-size characteristics of backshore beach deposits and dune/ridge sands are very similar.
519 They differ from the swash deposits in having a reduced presence of coarse grains and a better
520 sorting (Fig. 7). These properties indicate that aeolian processes likely have been in play in the
521 development of backshore deposits and dune ridges.

522

523 The grain-size variability in shore-normal direction along Transect A (Appendix B, Fig. B2) is
524 very similar to that of surficial samples taken at the current beach at Playa Estrella. Samples
525 from core 197 (Fig. B2, 0.04 km) reflect shore-normal sorting processes and demonstrate a
526 coarsening-upward sequence with strongly negatively skewed relatively fine sandy deposits at -4
527 m+MSL, likely deposited in the nearshore zone (Fig. 7a). These deposits are covered by a few
528 meters of fine sand with grain-size parameters resembling the surficial samples from the swash
529 zone (Fig. 7a), consistent with Walther's Law.

530

531 Samples from beach ridges formed during Phase 3B (Figs. 4b and B2, 3.5 km) are strikingly
532 different from the general pattern (Fig. 7b), with a higher contribution of well-sorted fine to
533 medium sand, likely related to an increased availability of reworked sand due to the erosion of
534 the SP y SP promontory. The same process is likely responsible for the coarser grain sizes of the
535 aeolian sand samples from the youngest ridge collected 10 km west of the still eroding SP y SP
536 promontory (Fig. 6).

537

538 **4.4 Internal architecture**

539 Despite the high signal attenuation, which limited the depth of investigation in various areas, the
540 GPR measurements clearly show strong seaward-dipping reflectors in all transects (Fig. 8), with
541 slopes between 2 and 5° (Fig. 4b and 8). Since all GPR transects were oriented perpendicular to
542 the ridges, these angles are close to the actual angles. The values are similar to dipping angles
543 reported by Psuty (1967) for beach deposits elsewhere along this coast. The largest slope angles
544 are preferentially associated with more elevated beach ridges. No reflections hinting at
545 interrupting erosional surfaces are apparent, and strong landward-dipping reflectors were rarely
546 encountered in the GPR-surveyed transects.

547



548 The top of the foreshore deposits is located around 0.8 m+MSL (Fig. 8). At depths between 1
549 and 2 m-MSL, the slopes of the upper-shoreface deposits start to decrease. Reflection
550 terminations (e.g. at $x = 40$ m and $y = 60-80$ ns; $x = 85$ m and $y = 35$ ns in Fig. 8) suggest the
551 periodic welding of bars onto the beach face (i.e. beach progradation by bar accretion). The few
552 landward-dipping reflections seen at the top of the beach sequence presumably relate to the infill
553 of a large runnel that formed when a swash bar merged with the beach.

554

555 The GPR results compare well with the extensive investigations conducted at the fine sandy
556 swash-built beach ridges at St. Vincent Island, Florida (Forrest, 2007), confirming the
557 prominence of swash deposits in beach-ridge sequences formed under microtidal conditions and
558 relatively low wave impact. It is hard to distinguish the aeolian radar facies from that of the
559 lithologically similar beach deposits, with the only useful indicator being the termination of
560 seaward-dipping foreshore reflections (red dashed line in Fig. 8). The absence of significant
561 internal erosional surfaces suggests that the ridges formed quickly or at least continuously,
562 uninterrupted by significant coastal-erosion events. Landward-dipping overwash deposits, as
563 described by Psuty (1967; 1969), are not evident in our selected GPR transects (nor did LiDAR
564 data support their presence in the promontory parts of the beach-ridge complexes). The
565 landward-dipping structures in Fig. 8 are situated too deep in the subsurface to be interpreted as
566 overwash deposits.

567

568 **4.5 Composition and source of beach-ridge sands**

569 The major-element compositions of relatively large sand-sized volcanic glass shards and pumice
570 fragments (250-1500 μm) and a pumice clast of 1.5 cm, isolated from beach-ridge samples along
571 Transect A, are reported in Table A3. The major-element composition is similar to that of the
572 Late Pleistocene Los Chocoyos tephra (Kutterolf et al., 2008), and is significantly different from
573 any of the late-Holocene tephra of El Chichón volcano (Fig. 9) (Nooren et al., 2017). It is
574 therefore inferred that Los Chocoyos ignimbrites have been an important sediment source for the
575 Usumacinta-Grijalva delta. They were emplaced during a mega-eruption at Atitlán volcanic
576 centre around 84,000 years ago (Drexler et al., 1980), which produced an estimated 150 to 160
577 km^3 Dense-Rock Equivalent (DRE) of tephra fall and some 120 km^3 DRE of pyroclastic flow
578 deposits (Rose et al., 1987). It is the only Late-Pleistocene volcanic eruption that deposited
579 voluminous tephra north of the Motagua River valley (Fig. 1a; Koch and McLean, 1975). The
580 Los Chocoyos pyroclastic flow deposits reach thicknesses of more than 200 m, and have been
581 found well into the watersheds of the Grijalva and Usumacinta Rivers (Instituto Geográfico
582 Nacional, 1970; Koch and McLean, 1975; Rose et al., 1987; Sánchez-Núñez et al., 2015). We
583 estimate that approximately 3 % and 16 % of the pyroclastic flow deposits were deposited in the
584 Grijalva and Usumacinta watersheds, respectively. In the steep and poorly vegetated terrain,
585 these volcanoclastic deposits are vulnerable to erosion and particularly prone to mass transport by
586 landslides (Harp et al., 1981). It is therefore not surprising that abundant volcanoclastic minerals
587 and glass shards (Solís-Castillo et al., 2013) were found in Holocene levee deposits of the
588 Usumacinta River at Tierra Blanca (Fig. 1a), reflecting reworked Los Chocoyos tephra, as
589 geochemical and micromorphological evidence suggests (Table A3, (Cabadas-Báez et al., in
590 press).

591 The heavy-mineral analyses confirm the presence of volcanoclastic material within the beach-
592 ridge sands. The non-opaque heavy minerals are dominated by green and brown amphiboles,
593 clinopyroxene, titanite and epidote, whereas the opaque heavy minerals are dominated by
594 titanomagnetite.

595



596 **4.6 Beach-ridge elevation**

597 The temporal variability in beach-ridge elevation along the fifteen cross-normal ribbon-shaped
598 elevation transects representing Phases 2 and 3 is demonstrated in Fig. 10. Most noticeable are
599 the high-amplitude elevation changes along Transect B during Phase 2, and the relatively low
600 standard deviations during periods in which elevated beach ridges were formed. Overall, mean
601 swale elevations along Transects A, B and C show a continuously increasing trend of about 0.3
602 mm/yr (Fig. 10), which is in line with expected long-term rate of relative sea-level (RSL) rise in
603 the southern Gulf of Mexico area, and comparable to those of the reconstruction of RSL rise
604 made by Gischler and Hudson (2004) for Belize. The estimated depths of pedogenic
605 decalcification (Figs. 3a and 3b) also supports this RSL curve, but further analyses are needed
606 for better refinement. We found no evidence for a mid-Holocene RSL high-stand followed by a
607 2-m drop during the late Holocene (e.g. Stapor et al., 1991; Tanner, 1992; Morton et al., 2000;
608 Blum et al., 2003). Rather, our observations are in accord with more recent RSL reconstructions
609 for the northern Gulf of Mexico coast that show a gradual rate of RSL rise during the late
610 Holocene (Törnqvist et al., 2004; Milliken et al., 2008; Donnelly and Giosan, 2008).

611

612 **4.7 Volumetric growth rate of the beach-ridge plain**

613 The total average late-Holocene sediment-accumulation rate was estimated by simply dividing
614 the total volume of beach-ridge deposits along the system's 150 km length by the duration of
615 beach-ridge formation. Assuming an average thickness of 10 ± 2 m, the overall average
616 accumulation rate over the period 1800 BCE until today has been 2.3–3.5 million m^3/yr .
617 Accumulation rates along Transects A, B and C range between 16 and 54 $\text{m}^3/\text{m}/\text{yr}$ (Table 2).

618

619 The calculated average accumulation rate is exceptionally high compared to those reported for
620 other large beach-ridge systems, such as 0.05 million m^3/yr at Guichen Bay, Australia (Bristow
621 and Pucillo, 2006), 0.14 million m^3/yr at Keppel Bay, Australia (Brooke et al., 2008a) and 1.7
622 million m^3/yr at Kujukuri, Japan (Tamura et al., 2010). As these systems are much shorter than
623 the Usumacinta-Grijalva plain, accumulation rates are more similar when expressed in $\text{m}^3/\text{m}/\text{yr}$.
624 For two other large beach-ridge systems with detailed chronological control we estimate
625 accumulation rates of 0.92 million m^3/yr (Nayarit, Mexico; using cross sections in Curray et al.,
626 1969), and 1.4 million m^3/yr (Katwijk, the Netherlands; using sections in Cleveringa, 2000).

627

628 Average aeolian accretion rates along Transects A, B and C range between 1.2 and 6.1 $\text{m}^3/\text{m}/\text{yr}$
629 (Table 2), with relatively high values along Transect B during Phase 2 and along Transect A
630 during Phase 3B. Rates are much higher than the average long-term aeolian accretion rates of 0.1
631 – 0.6 $\text{m}^3/\text{m}/\text{yr}$ for three beach-ridge plains in southeastern Australia (Oliver, 2016) but are
632 relative low compared to average long-term accretion rates for larger-scale foredunes, which
633 roughly vary between 5 and 20 $\text{m}^3/\text{m}/\text{yr}$ (e.g. Aagaard et al., 2004; Ollerhead et al., 2013;
634 Keijsers et al., 2014).

635

636 Aeolian accretion rates are ca. 5-20% of the total volumetric growth rate of the beach-ridge plain
637 (Table 2), comparable to the 10.5% inferred for the Moruya beach plain, Australia (Oliver,
638 2016). Aeolian processes therefore play a minor role in beach-plain sediment accretion.

639 We found a relatively large contribution of aeolian accretion (20-30% of total beach-ridge
640 accretion) for beach ridges formed along Transect B between approximately 1800 BCE and 30
641 CE (Phase 2), which could be an indication of stronger easterly trade winds during this time.

642



643 **4.8 Evolution of the beach-ridge plain**

644 The new chronological, geomorphological and sedimentary data enabled us to reconstruct the
645 three-phased development of the beach ridge complex in considerably more detail than previous
646 researchers.

647
648 The oldest part of the beach-ridge sequence (Phase 1) has been most completely preserved on the
649 inland side of the barrier complex, southwest of the current confluence of the Grijalva and
650 Usumacinta Rivers (Tres Brazos, Fig. 2b). Here, beach ridges are partly covered by organic-rich
651 back-barrier marsh deposits that locally reach thicknesses of up to 4 m (e.g. core 307; Fig. 3b).
652 To the east of Tres Brazos (Fig. 2b), no Phase 1 beach-ridge topography is discernible from the
653 DEM. Any Phase 1 ridges were likely eroded over time by the migrating Usumacinta River. Our
654 oldest age of 4248 ± 90 BCE (at 1σ) for freshwater organic deposits (sampled in core 307, Fig.
655 3b), post-dates the onset of coastal progradation in the study area. This organic unit formed after
656 the oldest beach ridges had developed, suggesting that the inception of the Usumacinta-Grijalva
657 beach-ridge plain (i.e. the onset of Phase 1), marking the transition from transgressive to
658 regressive conditions, probably occurred centuries earlier (ca. 4500 BCE).

659
660 Relatively coarse-grained beach ridges, inferred to be supplied with sediment by a branch of the
661 Grijalva River, accreted during Phase 1A along the inland part of Transect B (Fig. 5a). This set
662 of beach ridges formed until 2800 BCE, at a time when RSL was several meters lower than
663 today. Nowadays, only the most elevated beach ridges formed during that phase protrude from
664 the marshy plain.

665 During Phase 1B, which lasted until 1800 BCE, the Usumacinta River system increasingly
666 supplied relatively fine sediment to the area, as its SP y SP distributary developed. The inland
667 part of Transect A shows that the new promontory at the mouth of the SP y SP did not
668 immediately developed the characteristics of a mature beach-ridge plain. At core location PP1
669 and at Pozpetr (Fig. 3a), only clayey estuarine and organic flood-basin deposits occur. The first
670 beach-ridge sand body only starts near core 336. The few linear structures in the DEM that are
671 discernible further inland may represent chenier-like features (as tentatively indicated in Fig. 3a).
672 The Grijalva River system continued to influence beach-ridge formation in the area of Transect
673 B. During Phase 1B it made use of the 'Popal Grande palaeochannel' (cf. Psuty, 1967), which
674 was active between approximately 2800 and 2100 BCE (Fig. 5).

675
676 During Phase 2 (1800 BCE – 150 CE), the SP y SP promontory further developed. Its relative
677 large acute angles between beach ridges and the present-day coastline (Fig. 2), indicate that
678 riverine sediment supply contributed significantly to the growing beach ridge complex. Fluvial
679 contributions from more easterly sources are improbable, because sizeable rivers have not been
680 present east of the SP y SP branch. In addition, calcareous biogenic sediments dominate in that
681 sector of the coastal-lagoonal plain, particularly east of Ciudad del Carmen (Fig. 1b). A marine
682 source area is unlikely as well, because surface sediments in front of the SP y SP river mouth are
683 predominantly composed of clay and fine silt (Ayala-Castañares and Gutiérrez-Estrada, 1990).
684 A possible marine source area for beach-ridge sands is the seabed in the western part of the study
685 area (Fig. 1b), but there is no known mechanism that could have moved vast amounts of
686 sediment against the dominant drift direction. A terrestrial contribution via longshore current,
687 sourced from the Grijalva River mouth, is unlikely for the same reason: the necessary transport
688 path would be opposite the dominant drift direction. Moreover, the main distributaries of the
689 Grijalva River system at the time were positioned farther westward than at present (e.g. the
690 Pajonal and Blasillo palaeodistributaries described by Von Nagy (2003) (Fig. 1b). Towards the
691 end of Phase 2, a slight increase in acute angles of the beach ridges is seen about 5 km west of
692 the present main outlet (Fig. 2a). This local anomaly from the overall pattern indicates temporal



693 activation of a distributary river mouth at this location, which may be seen as a precursor of the
694 nearby main outlet active during Phase 3.

695
696 The break between Phases 2 and 3 is set at the marked increase in beach-ridge elevation, and at
697 regionally truncated beach ridges in the area near Transect B. These features indicate a major
698 reorganisation in the Grijalva and Usumacinta distributary network and river mouths. Around
699 150 CE, a major new delta promontory began to develop, that still is the joint outlet of the
700 Grijalva and Usumacinta rivers today. In its development, we distinguish three sub-phases.
701 During Phase 3A, the old SP y SP outlet was still functioning. At the end of Phase 3A, the
702 Usumacinta had fully avulsed towards its current location, terminating sediment delivery at the
703 old outlet. The age-distance model of Transect A2 (Fig. 4c) indicates that this latter avulsion
704 occurred around 1050 CE. The break between Phases 3A and B is marked by a shift in beach-
705 ridge orientations. West of the SP y SP abandoned outlet, elevated beach ridges are related to
706 increased sediment supply due to cannibalisation of the former promontory. Even today, the old
707 SP y SP promontory is still eroding, with current rates around 3.5 m/yr (Ortiz-Pérez, 1992; Ortiz-
708 Pérez et al., 2010).

709 The break between Phases 3B and 3C, placed at 1460 CE, is not related to river-outlet
710 repositioning and therefore morphometrically more arbitrary. It is reflected by moderate
711 increases in progradation rate (Table 2).

712

713

714 **5 Discussion**

715

716 **5.1 Beach-ridge-formation model**

717 Psuty (1965, 1967) suggested an important contribution of storm surges and related overwash to
718 the development of the Usumacinta-Grijalva beach ridges. Our GPR measurements revealed only
719 evidence for swash-built beach ridges with an aeolian cap on top, whereas typical landward-
720 dipping reflections from washovers have not been identified. In addition, the sandy deposits do
721 not include any exceptionally coarse sand layers within the upper part of the cores, and most of
722 the analysed sand samples from above MSL were characterised as aeolian in origin. The DEM of
723 the area shows little evidence of extreme storm events impacting the area; scour holes were only
724 identified along one beach ridge, formed around 1450 CE. Nevertheless, storms do play a role in
725 beach-ridge formation. Strong north-westerly winds during ‘Nortes’, for example, cause beach
726 erosion (West et al., 1969). Owing to a temporal reversal in the longshore-current direction, sand
727 is transported eastward and contributes to beach-ridge formation several months after the storm
728 event. Individual storms associated with the nearby passage of hurricanes will also lead to beach
729 erosion. In both cases foreshore recovery likely takes places within a few months after the
730 erosional event (Carter, 1986 and references therein).

731

732 The GPR data show that each beach ridge in the study area likely starts as a wave-built swash
733 bar, formed over a period of 7 - 19 years. Once stabilised and no longer subject to hydrodynamic
734 processes, subsequent wind processes create an aeolian cap on the ridge. Sand is blown in from
735 the adjacent beach, including the active intertidal swash bar (exposed during low tide). It is
736 trapped by pioneer vegetation, especially *Ipomoea pes-caprae*, that rapidly colonises the young
737 ridge. The final ridge elevation is determined by the length of the period that the ridge is located
738 next to the beach: the longer the ridge is exposed to aeolian sand deposition, the higher it
739 becomes. Consequently, high beach ridges arise when coastal propagation rate is low. Along
740 individual beach ridges, sections formed relatively close to an active river apex, where
741 progradation rates are high (Fig. 11b), are lower than those formed farther away (Fig. 11c),
742 where progradation rates are low. Apparently, reduced sediment supply leads to higher ridges.



743

744 **5.2 Beach-ridge elevation as a proxy of riverine sediment supply**

745 Beach-ridge elevation is negatively correlated with progradation rate, both in shore-normal
746 (Transect A, Phase 3A, Fig. 4c) and in a longshore direction (Fig. 11c). For periods when rivers
747 supplied most of the sediment stored in the beach-ridge system, we hypothesise that ridge
748 elevation along shore-normal transects may be used as a proxy of fluvial sediment supply
749 through time and space. Owing to the large storage capacity within the river basin, sediment
750 availability for fluvial transport is not a limiting factor. Peak river-discharge events and extended
751 periods of large supply translate into high progradation rates and lower ridges. Periods of
752 reduced supply during dry conditions, when rivers are less capable of transporting large amounts
753 of sand, result in higher ridges. Evidence for our hypothesis is provided by a comparison of the
754 beach-ridge morphology with independent information on climate in the catchments. We found
755 relatively high beach ridges along sections of Transects A, B and C formed during the period
756 between 810 – 950 CE (Fig. 10). This period, associated with the Maya Classic collapse, is well
757 known for the occurrence of multiple prolonged droughts in southern Mexico (cf. Hodell et al.,
758 1995) and Guatemala (cf. Wahl et al., 2014).

759

760 Direct sediment supply by rivers, however, is not always the main driver in coastal progradation.
761 Cannibalisation of abandoned promontories may generate abundant sandy sediment for
762 anomalously high sediment supply along the downdrift beach. A drastic increase in sediment
763 supply due to the erosion of the SP y SP promontory after the avulsion of the Usumacinta River
764 around 1050 CE resulted in increased availability of sand for aeolian reworking, triggering the
765 formation of relatively high beach ridges on both sites of the eroding SP y SP promontory (Figs.
766 4b and 10). Even ~1000 years after the avulsion that caused the Usumacinta River to join the
767 Grijalva River at Tres Brazos, coastal erosion at its former SP y SP apex is still ongoing. This
768 process is obscuring the relationship between direct fluvial sediment supply and beach-ridge
769 elevation, but can be recognised as a separate force because it caused major changes in geometry
770 and orientation of beach ridges (Fig. 2a), as well as clear changes in grain-size characteristics
771 (Figs. 4b and 5b).

772

773 Detecting changes in fluvial sediment supply from beach ridge elevation differences requires that
774 there are no major changes in wave and wind climate affecting the signal. Such changes in wave
775 and wind climate should be reflected in significant changes in the granulometric parameters of
776 the deposited beach ridge sand. After normalising for the effects of new river-mouth initiation
777 and old promontory abandonment, we find only minor remaining granulometric differences in
778 our study area. Comparison of modern deposits to the fossil beach deposits of Transect A (Fig.
779 B2) suggests that wind and wave climate (multi-decadal averaged) during the past 2000 years
780 (Phase 3) have been comparable to those of the present. In contrast, the different geometry of the
781 beach-ridge plain formed during the earlier Phase 2 (Fig. 11a) indicates that wind and wave
782 climate at that time were likely different from the situation today. During Phase 2, progradation
783 rates decreased relatively slowly with increasing distances from the SP y SP River mouth (Fig.
784 11b), and the promontory was less asymmetric than the promontory formed during Phase 3C at
785 the joint outlet of the Usumacinta and Grijalva Rivers. This difference can be explained by a
786 higher contribution of high-angle waves from the west in the construction of the delta
787 promontory, especially over the past 500 years, which is in agreement with model simulations of
788 delta development near river outlets (Ashton and Giosan, 2011). Such geometric changes can
789 thus occur without changes in sediment supply.

790 We speculate that the increased contribution of high-angle waves during Phase 3 is a possible
791 response to the increasingly frequent occurrences of north-westerly winds, probably related to a
792 stronger and more frequent contribution of cold fronts than before. During Phase 2, the



793 Intertropical Convergence Zone (ITCZ) was farther northward, and likely associated with
794 stronger easterly trade winds that could have caused the westward increase in aeolian accretion
795 rates during this time period (Fig. 11c).

796

797 **5.3 Beach-ridge periodicity**

798 Combining the age-distance modelling with the LiDAR-derived beach-ridge morphometrics
799 (Fig. 2a), it is evident that the development of past ridge-swale couplets took between 7 and 19
800 years (Table 2), and that the time interval for the formation of subsequent ridge-swale couplets
801 decreased with increasing progradation rate (Table 2). This relationship is apparent not only in
802 shore-normal transects marked by variable progradation rates, but also in a shore-parallel
803 direction, with beach ridges merging away from the river mouth supplying the sediment. It
804 corroborates a similar finding of Thompson (1992) for Lake Michigan beach ridges and indicates
805 that an allogenic cause of individual beach-ridge formation (e.g. periodic decimetre-scale lunar
806 or steric sea-level oscillations; Tanner, 1995), is unlikely. In this light, it should be noted that
807 long time series of water-level data from seven tide gauges along the southern Gulf of Mexico
808 (Salas-de-León et al., 2006) do not show any decadal periodicity. The inter-annual amplitude
809 variability is only a few centimetres, an order of magnitude lower than the intra-annual
810 amplitude range of 25 cm between a February low and an October high. We therefore conclude
811 that ridge-swale couplets at the study site are not formed in response to RSL oscillations. This
812 finding agrees with the findings of Tamura (2012) and Moore et al. (2016) that the formation of
813 individual ridge/swale couplets is driven by autocyclic processes (Moore et al., 2016).
814 Comparison with periodicities reported from other large beach-ridge systems (Fig. 12) indicates
815 that low periodicities (< 25 yr) indeed are generally found at sites with high progradation rates
816 (>1.5 m/yr).

817

818

819 **6 Conclusions**

820

821 Our study demonstrates the importance of riverine sediment supply in the formation of the
822 Usumacinta-Grijalva beach-ridge sequence, corroborating earlier geomorphological studies
823 (Psuty, 1965, 1967; West et al., 1969). In contrast to this earlier work, we propose a mechanism
824 of ridge formation without a significant role of storm surges and over-wash deposits. The fine
825 sandy beach ridges were mainly swash built, have an aeolian cap, and likely formed under fair-
826 weather conditions without the requirement of sea-level oscillation. Autocyclic processes
827 controlled the periodicity (7-19 yrs) in beach ridge formation. The relatively low periodicities are
828 related to high progradation rates (> ~1.5 m/yr) and reflect ample sediment supply. The
829 indicative meaning of beach-ridge periodicities in palaeoenvironmental reconstructions is
830 limited.

831

832 We estimate that sediment supply, distributed along 150 km of coastline, was roughly 2.3 – 3.5
833 million m³/yr, which is exceptionally large compared to that of other large beach-ridge
834 sequences. This can be attributed to extensive availability of easily erodible Los Chocoyos
835 ignimbrites in the headwater catchments of the Usumacinta River, given the abundance of
836 fragmented volcanic material derived from this unit in the beach ridge sands.

837

838 Our observations enabled us to subdivide the three main phases in the development of the beach-
839 ridge plain (Psuty, 1965, 1967; West et al., 1969) further into six sub-units, related to changes in
840 the configuration of the main river distributaries of the Usumacinta and Grijalva River system.
841 Combined ¹⁴C and OLS dating provided a robust and consistent chronological framework for



842 these phases, which substantially improved the existing chronology based on radiocarbon-dated
843 shell material (Aguayo et al., 1999).

844

845 Our analyses show that during periods when the Usumacinta River was the main supplier of
846 sandy sediments to the coast, changes in river discharge determined sediment availability,
847 progradation rate, and the final elevation of the beach ridges. Since the river discharge is directly
848 related to rainfall in the river catchment, beach ridge elevation may be an excellent proxy for
849 temporal changes in regional-scale precipitation.

850

851

852 **Acknowledgements**

853

854 We thank INEGI, Mexico for the generous provision of the LiDAR data, and Hector V. Cabadas-
855 Báez for kindly supplying the major-element data of glass shards recovered from levee deposits
856 at Tierra Blanca. Elise van Winden, Jesse Hennekam and Ryan Nagelkirk provided field support
857 and Salomon Kroonenberg offered valuable advice. This research is supported by the
858 Netherlands Organisation for Scientific Research (NWO grant 821.01.007). Remke van Dam
859 acknowledges support from the Michigan Space Grant Consortium.

860

861

862 **References**

863

864 Aagaard, T., Davidson-Arnott, R., Greenwood, B., and Nielsen, J.: Sediment supply from
865 shoreface to dunes: linking sediment transport measurements and long-term morphological
866 evolution, *Geomorphology*, 60, 205-224, 2004.

867

868 Administración Portuaria Integral de Dos Bocas S.A. de C.V.: Manifestación de Impacto
869 Ambiental Modalidad Particular; Construcción de Escolleras y del Dragado del Canal de Acceso
870 del Puerto de Frontera, Tabasco. Administración Portuaria Integral de Dos Bocas S.A. de C.V.,
871 Paraíso, Tabasco, México, 258 pp., 2005.

872

873 Aguayo, J.E., Gutiérrez-Estrada, M.A., Araujo-Mendieta, J., Sandoval-Ochoa, J.H.,
874 and Vázquez-Gutiérrez, F.: Geodinámica Holocénica y reciente del sistema
875 fluvio deltáico Grijalva-Usumacinta, suroeste del Golfo de México. *Revista de la*
876 *Sociedad Mexicana de Historia Natural* 49, 29-44, 1999.

877

878 Aitken, M.J., 1998: *An Introduction to Optical Dating: The Dating of Quaternary Sediments by*
879 *the Use of Photon-Stimulated Luminescence*, Oxford, Oxford University Press, 267 pp., 1998.

880

881 Ashton, A.D., and Giosan, L.: Wave-angle control of delta evolution, *Geophysical Research*
882 *Letters*, 38, L13405, 2011.

883

884 Ayala-Castañares, A. and Gutiérrez-Estrada, M.: Morfología y sedimentos superficiales de la
885 plataforma continental frente a Tabasco y Campeche, México, *Anales del Instituto de Ciencias*
886 *del Mar y Limnología*, UNAM, 17, 163–190, 1990.

887

888 Ballarini, M., Wallinga, J., Murray, A.S., Van Heteren, S., Oost, A.P., Bos, A.J.J., and Van Eijk,
889 C.W.E.: Optical dating of young coastal dunes on a decadal time scale, *Quaternary*
890 *Science Reviews*, 22(10–13), 1011–1017, 2003.

891



- 892 Balsillie, J.H.: William F. Tanner on Environmental Clastic Granulometry, Special Publication
893 40, Tallahassee, Florida Geological Survey. 145 pp., 1995.
894
- 895 Banco Nacional de Datos de Aguas Superficiales
896 http://www.conagua.gob.mx/CONAGUA07/Contenido/Documentos/Portada_BANDAS.htm
897 [conagua.gob.mx/Bandas/Bases_Datos_Presas/](http://www.conagua.gob.mx/Bandas/Bases_Datos_Presas/)
898
- 899 Blum, M.D., Sivers, A.E., Zayac, T., and Goble, R.J.: Middle Holocene Sea-Level and Evolution
900 of the Gulf of Mexico Coast. Gulf Coast Association of Geological Societies Transactions, 53,
901 64-77, 2003.
902
- 903 Bøtter-Jensen, L., Andersen, C.E., Duller, G.A.T., and Murray, A.S.: Developments in
904 radiation, stimulation and observation facilities in luminescence measurement,
905 Radiation Measurements, 37, 535–541, 2003.
906
- 907 Bristow, C.S., and Pucillo, K.: Quantifying rates of coastal progradation from sediment volume
908 using GPR and OSL: the Holocene fill of Guichen Bay, south-east South Australia,
909 Sedimentology, 53, 769–788, 2006.
910
- 911 Bronk Ramsey, C.: Bayesian analysis of radiocarbon Dates, Radiocarbon, 51, 337–360, 2009.
912
- 913 Bronk Ramsey, C.: Oxcal 4.2., <http://c14.arch.ox.ac.uk/oxcal.html>, 2016.
914
- 915 Brooke, B., Ryan, D., Pietsch, T., Olley, J., Douglas, G., Packett, R., Radke, L., and Flood, P.:
916 Influence of climate fluctuations and changes in catchment land use on Late Holocene and
917 modern beach-ridge sedimentation on a tropical macrotidal coast: Keppel Bay, Queensland,
918 Australia, Marine Geology, 251, 195–208, 2008a.
919
- 920 Brooke, B., Lee, R., Cox, M., Olley, J., and Pietsch, T.: Rates of Shoreline Progradation during
921 the Last 1700 Years at Beachmere, Southeastern Queensland, Australia, Based on Optically
922 Stimulated Luminescence Dating of Beach Ridges, Journal of Coastal Research, 24, 640–648,
923 2008b.
924
- 925 Cabadas-Báez, H.V., Solís-Castillo, B., Solleiro-Rebolledo, E., Sedov, S., Leonard, D., and
926 Teranishi-Castillo, K.: Reworked volcanoclastic deposits from the Usumacinta river, Mexico: A
927 serendipitous source of volcanic glass in Maya ceramics, Geoarchaeology, in press.
928
- 929 Carter, R.W.G.: The morphodynamics of beach-ridge formation: Magilligan, Northern Ireland,
930 Marine Geology, 73, 191-214, 1986.
931
- 932 Castillo, S., Pompa, J., and Moreno-Casasola, P.: Coastal sand dune vegetation of Tabasco and
933 Campeche, Mexico. Journal of Vegetation Science, 2, 73-88, 1991.
934
- 935 Cleveringa, J.: Reconstruction and modelling of Holocene coastal evolution of the western
936 Netherlands, PhD thesis Utrecht University, the Netherlands, 2000.
937
- 938 Cunningham, A.C., and Wallinga, J.: Realizing the potential of fluvial archives using robust OSL
939 chronologies, Quaternary Geochronology, 12, 98-106, 2012.
940



- 941 Cunningham, A.C., and Wallinga, J.: Selection of integration time-intervals for quartz OSL
942 decay curves, *Quaternary Geochronology*, 5, 657-666, 2010.
- 943
- 944 Curray, J.R., Emmel, F.J., and Crampton, P.J.S.: Holocene history of a strand plain, lagoonal
945 coast, Nayarit, Mexico. In: Ayala-Casteñares, A., Phleger, F.B. (Eds.), *Lagunas Costeras*, UN
946 Symposium. UNAM-UNESCO, Mexico, D.F, 63–100, 1969.
- 947
- 948 Donnelly, J.P. and Giosan, L.: Tempestuous highs and lows in the Gulf of Mexico, *Geology*, 36,
949 751-752, 2008.
- 950
- 951 Drexler, J.W., Rose, W.I., Sparks, R.S.J., and Ledbetters, M.T.: The Los Chocoyos Ash,
952 Guatemala: A major stratigraphic marker in middle America and in three ocean basins,
953 *Quaternary Research*, 13, 327–345, 1980.
- 954
- 955 Duller, G.A.T.: Distinguishing quartz and feldspar in single grain luminescence measurements,
956 *Radiation Measurements*, 37, 161–165, 2003.
- 957
- 958 Folk R.L., and Ward, W.C.: Brazos River bar: a study in the significance of grain size
959 parameters, *Journal of Sedimentary Petrology*, 27, 3–26, 1957.
- 960
- 961 Forrest, B.M.: Evolution of the Beach Ridge Strandplain on St. Vincent Island, Florida, Thesis,
962 Florida State University, 269 pp., 2007.
- 963
- 964 Forsyth, A.J., Nott, J., and Bateman, M.D., Beach ridge plain evidence of a variable late-
965 Holocene tropical cyclone climate, North Queensland, Australia, *Palaeogeography*,
966 *Palaeoclimatology*, *Palaeoecology*, 297, 707–716, 2010.
- 967
- 968 Galbraith, R.F., Roberts, R.G., Laslett, G.M., Yoshida, H., and Olley, J.M.: Optical dating
969 of single and multiple grains of quartz from Jinnium rock shelter, Northern Australia: part I,
970 experimental design and statistical models, *Archaeometry*, 41, 339–364, 1999.
- 971
- 972 Gallego-Fernández, J.B., and Martínez, M.L.: Environmental filtering and plant functional types
973 on Mexican foredunes along the Gulf of Mexico. *Ecoscience*, 18(1), 52-62, 2011.
- 974
- 975 Garrison Jr., J.R., Mestas-Nuñez, A.M., Williams, J.R., and Lumb, L.M.: Can beach dune ridges
976 of the Texas Gulf Coast preserve climate signals?, *Geo-Mar. Lett.*, 32, 241–250, 2012.
- 977
- 978 Garrity, C.P., and Soller, D.R.: Database of the Geologic Map of North America; adapted from
979 the map by J.C. Reed, Jr. and others (2005): U.S. Geological Survey Data Series 424
980 [<https://pubs.usgs.gov/ds/424/>], 2009.
- 981
- 982 Gischler, E., and Hudson, J.H.: Holocene development of the Belize barrier reef, *Sediment.*
983 *Geol.*, 164, 223-236, 2004.
- 984
- 985 Guedes, C.C.F., Giannini, P.C.F., Nascimento Jr., D.R. Sawakuchi, A.O., Tanaka, A.P.B., and
986 Rossi, M.G.: Controls of heavy minerals and grain size in a holocene regressive barrier (Ilha
987 Comprida, southeastern Brazil), *Journal of South American Earth Sciences*, 31, 110-123, 2011.
- 988
- 989 Guérin, G., Mercier, N., and Adamiec, G.: Dose-rate conversion factors: update: *Ancient TL*, 29,
990 5-8, 2011.



- 991
992 Harp, E.L., Wilson, R.C., Wieczorek, G.F.: Landslides from the February 4, 1976, Guatemala
993 earthquake, US Geological Survey, Prof. Paper 1024-A, 1981.
994
995 Hijmans, R.J., Cameron, S.E., Parra, J.L., Jones, P.G., and Jarvis, A.: Very high resolution
996 interpolated climate surfaces for global land areas. *International Journal of Climatology*, 25,
997 1965-1978, 2005.
998
999 Hinojosa, C., Nooren, K., Solleiro-Rebolledo, E., Sedov, S., Salazar, O.: Soil development on a
1000 beach ridge chronosequence in the Gulf of Mexico coastal plain and its relation to the ancient
1001 land use, *Quaternary International*, 418, 180-194, 2016.
1002
1003 Hodell, D.A., Curtis, J.H., and Brenner, M.: Possible role of climate in the collapse of
1004 Classic Maya civilization, *Nature*, 375(6530), 391–394, 1995.
1005
1006 Instituto Geográfico Nacional: Mapa Geológico de Guatemala a escala 1:500,000, 1970.
1007
1008 Jol, H.M., Smith, D.G., and Meyers, R.A.: Digital ground penetrating radar (GPR): a new
1009 geophysical tool for coastal barrier research (examples from the Atlantic, Gulf and Pacific
1010 Coasts, U.S.A.), *Journal of Coastal Research*, 12, 960–968, 1996.
1011
1012 Jom Morán, S.A.: Medición batimétrica para determinar el volumen de material sedimentado
1013 acumulado durante el tiempo de servicio del embalse Pueblo Viejo, de la central hidroeléctrica
1014 Chixoy. Msc thesis, Universidad de San Carlos de Guatemala, 2010.
1015
1016 Keijsers, J.G.S., Poortinga, A., Riksen, M.J.P.M., and Maroulis, J.: Spatio-Temporal Variability
1017 in Accretion and Erosion of Coastal Foredunes in the Netherlands: Regional Climate and Local
1018 Topography. *PLoS ONE* 9(3), e91115, doi:10.1371/journal.pone.0091115, 2014.
1019
1020 Koch, A.J., and McLean, H.: Pleistocene tephra and ash-flow deposits in the volcanic highlands
1021 of Guatemala. *Geological Society of America Bulletin*, 86, 529-541, 1975.
1022
1023 Komar, P.D.: The entrainment, transport and sorting of heavy minerals by waves and currents,
1024 *Developments in Sedimentology*, 58, 3–48, 2007.
1025
1026 Kutterolf, S., Freundt, A., Pérez, W., Mörz, T., Schacht, U., Wehrmann, H., and Schmincke, H.-
1027 U.: Pacific offshore record of plinian arc volcanism in Central America: 1. Along-arc
1028 correlations: *Geochemistry, Geophysics, Geosystems*, 9, Q02S01, 2008.
1029
1030 López, G.I., and Rink, W.J.: New quartz optical stimulated luminescence ages for beach ridges
1031 on the St. Vincent Island Holocene strand plain, Florida, United States. *Journal of Coastal*
1032 *Research*, 24, 49–62, 2008.
1033
1034 Marrufo, R.J., and González, F.J.: Use of Lidar Data in Floodplain Risk Management Planning:
1035 The Experience of Tabasco 2007 Flood. In *Advances in Geoscience and Remote Sensing*,
1036 INTECH, chapter 32, 659-678, 2012.
1037
1038 May, J.H., Wells, S.G., Cohen, T.J., Marx, S.K., Nanson, G.C., and Baker, S.E.: A soil
1039 chronosequence on Lake Mega-Frome beach ridges and its implications for late
1040 Quaternary pedogenesis and paleoenvironmental conditions in the drylands of



- 1041 southern Australia, *Quaternary Research*, 83, 150-165, 2015.
1042
1043 McCave, I.N.: Grain-size trends and transport along beaches: example from eastern England.
1044 *Marine Geology*, 28, M43-M51, 1978.
1045
1046 Milana, J.P., Conforti Ferreira Guedes, C., and Valdez Buso, V.: The coastal ridge sequence at
1047 Rio Grande do Sul: A new geoarchive for past climate events of the Atlantic coast of southern
1048 Brazil since the mid Holocene, *Quaternary International*, in press.
1049
1050 Milliken, K.T., Anderson, J.B., and Rodriguez, A.B.: A new composite Holocene sea-level curve
1051 for the northern Gulf of Mexico, *The Geological Society of America, Special Paper 443*, 1-11,
1052 2008.
1053
1054 Minderhoud, P., Cohen, K.M., Toonen, W.H.J., Erkens, G., and Hoek, W.Z.: Improving age-
1055 depth models of fluvio-lacustrine deposits using sedimentary proxies for accumulation rates,
1056 *Quaternary Geochronology*, 33, 35-45, 2016.
1057
1058 Mook, W.G., and Van der Plicht, J.: Reporting ^{14}C activities and concentrations, *Radiocarbon*,
1059 41, 227-239, 1999.
1060
1061 Moore, L.J., Durán Vinent, O., and Ruggiero, P.: Vegetation control allows autocyclic formation
1062 of multiple dunes on prograding coasts, *Geology*, 44(7), 559–562, 2016.
1063
1064 Morton, R.A., Paine, J.G., and Blum, M.D.: Responses of stable bay-margin and barrier-island
1065 systems to Holocene sea-level highstands, western Gulf of Mexico, *Journal of Sedimentary*
1066 *Research*, 70, 478–490, 2000.
1067
1068 Muñoz-Salinas, E. Castillo, M., Sanderson, D., Kinnaird, T., and Cruz-Zaragoza, E.: Using three
1069 different approaches of OSL for the study of young fluvial sediments at the coastal
1070 plain of the Usumacinta–Grijalva River Basin, southern Mexico, *Earth Surface Processes and*
1071 *Landforms*, 41, 823–834, 2016.
1072
1073 Murray-Wallace, C.V., Banerjee, D., Bourman, R.P., Olley, J.M. and Brooke, B.P.: Optically
1074 stimulated luminescence dating of Holocene relict foredunes, Guichen Bay, South Australia,
1075 *Quaternary Science Reviews*, 21, 1077-1086, 2002.
1076
1077 Murray, A.S., and Wintle, A.G.: The single aliquot regenerative dose protocol: potential for
1078 improvements in reliability. *Radiation Measurements*, 37, 377-381, 2003.
1079
1080 Nielsen, A., Murray, A.S., Pejrup, M., and Elberling, B.: Optically stimulated luminescence
1081 dating of a Holocene beach ridge plain in Northern Jutland, Denmark, *Quaternary*
1082 *Geochronology*, 1, 305–312, 2006.
1083
1084 Nielsen, A.H., Elberling, B., and Pejrup, M.: Soil development rates from an optically stimulated
1085 luminescence-dated beach ridge sequence in Northern Jutland, Denmark, *Canadian Journal of*
1086 *Soil Science*, 90(2), 295-307, 2010.
1087
1088 Nieuwenhuysse, A., and Kroonenberg, S.B.: Volcanic origin of Holocene beach ridges
1089 along the Caribbean coast of Costa Rica, *Marine Geology*, 120, 13–26, 1994.
1090



- 1091 Nooren, K., Hoek, W.Z., Van der Plicht, H., Sigl, M., Van Bergen, M.J., Galop, D., Torrescano-
1092 Valle, N., Islebe, G., Huizinga, A., Winkels, T., and Middelkoop, H.: Explosive eruption of El
1093 Chichón volcano (Mexico) disrupted 6th century Maya civilization and contributed to global
1094 cooling, *Geology*, 45(2), 175-178, 2017.
- 1095
1096 Nott, J., Smithers, S., Walsh, K., Rhodes, E.: Sand beach ridges record 6000 year history of
1097 extreme tropical cyclone activity in northeastern Australia, *Quaternary Science Reviews*, 28,
1098 1511–1520, 2009.
- 1099
1100 Nott, J.: A 6000 year tropical cyclone record from Western Australia, *Quaternary Science*
1101 *Reviews*, 30, 713–722, 2011.
- 1102
1103 Oliver, T.S.N.: Holocene depositional history of three coastal sand ridge plains, southeastern
1104 Australia. Doctor of Philosophy thesis, School of Earth and Environmental Sciences, University
1105 of Wollongong, Australia, 216 pp., 2016.
- 1106
1107 Oliver, T.S.N., Dougherty, A.J., Gliganic, L.A., and Woodroffe, C.D.: Towards more robust
1108 chronologies of coastal progradation: optically stimulated luminescence ages for the coastal plain
1109 at Moruya, south-eastern Australia, *The Holocene*, 25, 536–546, 2015.
- 1110
1111 Ollerhead, J., Davidson-Arnott, R., Walker, I.J., and Mathew, S.: Annual to decadal
1112 morphodynamics of the foredune system at Greenwich Dunes, Prince Edward Island, Canada,
1113 *Earth Surface Processes and Landforms*, 38, 284-298, 2013.
- 1114
1115 Ortíz-Pérez, M.A.: Retroceso reciente de la línea ed costa del frente deltáico del Río San Pedro,
1116 Campeche-Tabasco, *Investigaciones Geográficas*, 25, 7-24, 1992.
- 1117
1118 Ortíz-Pérez, M.A., Hernández-Santana, J.R., Figueroa Mah Eng, J.M., and Gama Campillo, L.:
1119 Tasas del avance transgresivo y regresivo en el frente deltaico tabasqueño: en el período
1120 comprendido del año 1995 al 2008. In: *Vulnerabilidad en las zonas costeras mexicanas ante el*
1121 *cambio climático*, Botello, A.V., Villanueva-Fragoso, S., Gutiérrez, J., and Rojas Galaviz, J.L.
1122 (eds.), UNAM-INE, 305-324, 2010.
- 1123
1124 Otvos, E.G.: Beach Ridges — definitions and significance, *Geomorphology*, 32, 83–108, 2000.
- 1125
1126 Otvos, E.G.: Coastal barriers, Gulf of Mexico: Holocene evolution and chronology, *Journal of*
1127 *Coastal Research*, SI(42), 141-163, 2005.
- 1128
1129 Padilla, R.J., and Sánchez: Evolución geológica del sureste mexicano desde el Mesozoico
1130 al presente en el contexto regional del Golfo de México, *Boletín de la Sociedad Geológica*
1131 *Mexicana*, Tomo LIX(1), 19-42, 2007.
- 1132
1133 Prescott, J.R., and Hutton, J.T.: Cosmic ray distributions to dose rates for luminescence and ESR
1134 dating: large depths and long-term variations, *Radiation Measurements*, 23, 497–500, 1994.
- 1135
1136 Psuty, N.P.: Beach ridge development in Tabasco, Mexico, *Annals Association of American*
1137 *Geographers*, 55, 112–124, 1965.
- 1138
1139 Psuty, N.P.: *The Geomorphology of Beach Ridges in Tabasco, Mexico*, Coastal Studies Series
1140 18, Louisiana State University Press, Baton Rouge, USA, 51 pp., 1967.



- 1141
1142 Ramos J., Marrufo L., and González F.J.: Use of Lidar Data in Floodplain Risk Management
1143 Planning: The Experience of Tabasco 2007 Flood In: Jedlovec, G. (ed.), *Advances in Geoscience*
1144 and Remote Sensing, Intech, doi: 10.5772/8322, 2009.
1145
1146 Reimann, T., Tsukamoto, S., Harff, J., Osadczuk, K., and Frechen, M.: Reconstruction of
1147 Holocene coastal foredune progradation using luminescence dating — An example from the
1148 Świna barrier (southern Baltic Sea, NW Poland), *Geomorphology*, 132, 1–16, 2011.
1149
1150 Reimer, P.J., et al.: IntCal13 and Marine13 radiocarbon age calibration curves 0–50,000 years
1151 cal BP, *Radiocarbon*, 55, 1869–1887, 2013.
1152
1153 Remillard, A.M., Buylaert, J.-P., Murray, A.S., St-Onge, G., Bernatches, P., and Hetu, B.: Quartz
1154 OSL dating of the late Holocene beach ridge from the Magdalen Islands (Quebec, Canada),
1155 *Quaternary Geochronology*, 30, 264–269, 2015.
1156
1157 Rink, W.J. and López, G.I.: OSL-based lateral progradation and aeolian sediment accumulation
1158 rates for the Apalachicola Barrier Island Complex, North Gulf of Mexico, Florida,
1159 *Geomorphology*, 123, 330–342, 2010.
1160
1161 Rose, W.I., Newhall, C.G., Bornhorst, T.J., Self, C.: Quaternary silicic pyroclastic deposits of
1162 Atitlán Caldera, Guatemala, *Journal of Volcanology and Geothermal Research*, 33, 57–80, 1987.
1163
1164 Salas-de-León, D.A., Monreal-Gómez, M.A., Salas-Monreal, D., Riverón-Enzástiga, M.L., and
1165 Sánchez-Santillan, N.L.: Inter-annual sea level variability in the southern Gulf of Mexico
1166 (1966–1976), *Geophysical Research Letters*, 33, L08610, 2006.
1167
1168 Salas-de-León, D.A., Monreal-Gómez, M.A., Miguel Díaz-Flores, M.A., Salas-Monreal, D.,
1169 Velasco-Mendoza, H., Riverón-Enzástiga, M.L., and Ortiz-Zamora, G.: Role of Near-Bottom
1170 Currents in the Distribution of Sediments within the Southern Bay of Campeche,
1171 Gulf of Mexico, *Journal of Coastal Research*, 24(6), 1487–1494, 2008.
1172
1173 Sánchez-Núñez, M.M., Macías, J.L., Saucedo, R., Zamorano, J.J., Novelo, D., Mendoza, M.E.,
1174 and Torres-Hernández, J.R.: Geomorphology, internal structure and evolution of alluvial fans at
1175 Motozintla, Chiapas, Mexico, *Geomorphology*, 230, 1–12, 2015.
1176
1177 Scheffers, A., Engel, M., Scheffers, S., Squire, P., Kelletat, D.: Beach ridge systems –
1178 archives for Holocene coastal events?, *Progress in Physical Geography*, 36(1), 5–37, 2012.
1179
1180 Solís-Castillo, B., Thiel, C., Cabadas-Báez, H., Solleiro-Rebolledo, E., Sedov, S., Terhorst, B.,
1181 Damm, B., Frechen, M., and Tsukamoto, S.: Holocene sequences in the Mayan Lowlands—A
1182 provenance study using heavy mineral distributions. *Eiszeitalter und Gegenwart Quaternary*
1183 *Science Journal*, 62, 84–97, 2013.
1184
1185 Stapor, F.W., Jr., Mathews, T.D., and Lindfors-Kearns, F.E.: Barrier-island progradation and
1186 Holocene sealevel history in southwest Florida, *Journal of Coastal Research*, 7, 815–838, 1991.
1187
1188 Tamura, T.: Beach ridges and prograded beach deposits as palaeoenvironment records, *Earth-*
1189 *Science Reviews*, 114, 279–297, 2012.
1190



- 1191 Tamura, T., Murakami, F., and Watanabe, K.: Holocene beach deposits for assessing
1192 coastal uplift of the northeastern Boso Peninsula, Pacific coast of Japan, Quaternary
1193 Research, 74, 227–234, 2010.
1194
- 1195 Tanner, W.F.: Origin of beach ridges and swales. *Marine Geology*, 129, 149–161, 1995.
1196
- 1197 Tanner, W.F.: Late Holocene sea-level changes from grain-size data: evidence from the Gulf of
1198 Mexico, *The Holocene*, 2, 249–254, 1992.
1199
- 1200 Taylor, M.J., and Stone, G.W.: Beach-ridges: a review, *Journal of Coastal Research*, 12,
1201 612–621, 1996.
1202
- 1203 Thompson, T.A.: Beach-ridge development and lake-level variation in southern Lake Michigan,
1204 *Sedimentary Geology*, 80, 305–318, 1992.
1205
- 1206 Törnqvist, T.E., Gonzalez, J.L., Newsom, L.A., van der Borg, K., de Jong, A.F.M., and Kurnik,
1207 C.W.: Deciphering Holocene sea-level history on the U.S. Gulf Coast: A high-resolution record
1208 from the Mississippi Delta: *Geological Society of America Bulletin*, 116, 1026–1039, 2004.
1209
- 1210 USGS: Shuttle Radar Topography Mission (SRTM) 1 Arc-Second Global dataset,
1211 <https://lta.cr.usgs.gov/SRTM1Arc>, 2009.
1212
- 1213 Van der Meene, E.A., Van der Staay, J., and Lay Hock, T.: The Van der Staay suction-corer – a
1214 simple apparatus for drilling in sand below groundwater table, *Rijks Geologische Dienst*,
1215 Haarlem, the Netherlands, 1979.
1216
- 1217 Van der Plicht, J., Wijma, S., Aerts, A.T., Pertuisot, M.H., and Meijer, H.A.J.: The Groningen
1218 AMS facility: status report, *Nuclear Instruments and Methods*, B172, 58-65, 2000.
1219
- 1220 Van Heteren, S., Fitzgerald, D.M., Mckinlay, P.A., and Buynevich, I.V.: Radar facies of
1221 paraglacial barrier systems: coastal New England, USA, *Sedimentology*, 45(1), 181–200, 1998.
1222
- 1223 Vespremeanu-Stroe, A., Preoteasa, L., Zăinescu, F., Rotaru, S., Croitoru, L., and Timar-Gabor,
1224 A.: Formation of Danube delta beach ridge plains and signatures in morphology, *Quaternary*
1225 *International*, 415, 268-285, 2016.
1226
- 1227 Von Nagy, C.: Of Meandering Rivers and Shifting Towns: Landscape Evolution and Community
1228 within the Grijalva delta. PhD thesis, Tulane University, USA, 1640 pp., 2003.
1229
- 1230 Visher, G.S.: Grain size distributions and depositional processes, *Journal of Sedimentary*
1231 *Petrology*, 39(3), 1074–1106, 1969.
1232
- 1233 Wahl, D., Byrne, R., and Anderson, L.: An 8700 year paleoclimate reconstruction from
1234 the southern Maya lowlands. *Quaternary Science Reviews*, 103, 19–25, 2014.
1235
- 1236 Wallinga, J.: Optically stimulated luminescence dating of fluvial deposits: a review, *Boreas*,
1237 31, 303–322, 2002.
1238
- 1239 West, R.C., Psuty, N.P., and Thom, B.G.: The Tabasco Lowlands of Southeastern Mexico,
1240 Technical Report 70, Louisiana State University, Baton Rouge, USA, 198 pp., 1969.



1241

1242

1243 **Figure captions**

1244

1245 Figure 1: (a) Location of the Usumacinta-Grijalva beach-ridge sequence (yellow) along the edge
1246 of the Holocene delta plain (blue) and the drainage basins of the two main rivers traversing the
1247 headlands of this delta (red outlines). Simplified geological map modified from Garrity and
1248 Soller (2009) and extent of Los Chocoyos pyroclastic flow deposits adopted from the geological
1249 map of Guatemala at scale 1:500,000 (Instituto Geográfico Nacional, 1970; Koch and McLean,
1250 1975; Rose et al., 1987; and Sánchez-Núñez et al., 2015). Elevated uplands above 500 m+MSL,
1251 outlined using the SRTM 1-arc-second dataset (USGS, 2009), are depicted in gray; (b) Overview
1252 of the Usumacinta-Grijalva delta and the three main phases of Holocene beach-ridge formation
1253 defined by Psuty (1965, 1967). The apexes of the two main rivers (yellow dots) are indicated
1254 with 25, 50 and 75 km equidistant lines (red lines). Nearshore distribution of coarse silty to
1255 gravelly surficial sediments after Ayala-Castañares and Gutiérrez-Estrada (1990). Surficial
1256 sediments from the remaining part of the continental shelf are composed of clay and fine silt.

1257

1258 Figure 2: (a) LiDAR-based DEM and location of studied transects, with the GPR transects in
1259 blue; (b) Main beach-ridge-formation phases, and locations of sediment cores (black) and of
1260 samples collected for OSL and AMS ^{14}C dating. Numbers 1-15 denote the fifteen cross-normal
1261 ribbon-shaped elevation transects, in the text referred to as B2-1, B2-2, etc.

1262

1263 Figure 3: Age-distance models for Transects A (a), and B (b). Indicated are the 1 sigma
1264 distribution for the model results using the P_{sequence} module in Oxcal 4.2 (Bronk Ramsey,
1265 2009). Sample locations of AMS ^{14}C (black squares) and OSL (red dots) samples are indicated,
1266 and projected samples are presented in italics. The calibrated ^{14}C ages are indicated with the full
1267 probability distribution and the OSL ages (red and yellow triangles) with their 1 sigma range.
1268 CaCO_3 content for selected core samples indicates pedogenic decalcification depth, used to
1269 estimate the position of MSL during beach-ridge formation. The dashed trendline is based on
1270 Gischler and Hudson's (2004) reconstruction of late-Holocene RSL.

1271

1272 Figure 4: (a) Core locations along Transect A2; (b) Median grain size of analysed sand samples,
1273 with associated shoreface-dipping angle; (c) Age-distance model (after Nooren et al., 2017) and
1274 OSL ages (red dots) (with 1 sigma probability).

1275

1276 Figure 5: (a) Reconstructed palaeoshorelines (ages in Year CE); (b) Median grain size (μm) of
1277 wave-formed and aeolian deposits (large and small dots, respectively).

1278

1279 Figure 6: (a) Shore-parallel variability in grain-size parameters of swash (red) and aeolian
1280 (black) facies. Vfs = very fine sand; fs = fine sand; ms = medium sand; cs = coarse sand.

1281

1282 Figure 7: (a) Grain-size variability along a beach-to-nearshore profile of surficial grab samples
1283 taken during fair-weather conditions in April 2013 at Playa Estrella (see Fig. 6 for location).
1284 Sand characteristics of beach core 197 (triangle; sample from -3.5 m+MSL), taken in 2012 at the
1285 same location are shown for comparison. The sand sample likely had its origin in the nearshore
1286 at a distance of 240 - 300 m from the contemporary low-tide line (here shown at 240 m),
1287 assuming a comparable beach profile during time of deposition. LWL and HWL are mean low
1288 and high water level; (b) Grain-size distribution of representative surficial sand samples from the
1289 beach profile, denoted by coloured circles in Fig. 7a.

1290



1291 Figure 8. Processed GPR data and interpretation for two closely spaced relatively elevated beach
1292 ridges along Transect A (see Fig. 2a and 3a for location), collected using a GSSI system with
1293 250MHz shielded antennas. Processing steps included signal dewow to remove low-frequency
1294 content, a custom gain function to amplify deeper reflections, background removal below the
1295 direct waves, and topographic correction. Time-to-depth conversion for the elevation axis was
1296 based on velocities of 0.125 and 0.06 m/ns above and below the water table, respectively. The
1297 position of the water table at 0.2 m+MSL (blue dashed line) was drawn on the basis of changes
1298 in reflection characteristics, and confirmed by observations from core 72 (black arrow). Here, the
1299 water table was positioned at 2.2 m below the land surface. Highlighted in the interpretation are
1300 foreshore and shoreface deposits (black dipping lines), the transition from foreshore to backshore
1301 and/or aeolian deposits at 0.8 m+MSL (red dashed line), and some landward-dipping structures
1302 (orange lines) possibly related to infill of a large former runnel. The curved reflections around
1303 110 m (40 ns and deeper) are caused by surface scattering off a large nearby tree that was passed
1304 while moving the GPR along the transect.

1305

1306 Figure 9: SiO₂ - CaO diagram for analysed volcanic glass shards, plotted along with
1307 compositional characteristics of El Chichón (Nooren et al., 2017) and Los Chocoyos tephra
1308 (Kutterolf et al., 2008). Data points represent averages for 5-12 particles (bars are 1 sigma).
1309 The SiO₂ - CaO composition of volcanic glass shards recovered from Usumacinta levee deposits
1310 at Tierra Blanca III (Cabadas-Báez et al., 2017) are indicated for comparison. We refer to table A3 for
1311 all major element data. Inset: Thin section of pumice and volcanic glass shards recovered from the
1312 beach-ridge sands (core 197, sample from 80 cm below surface). Notice elongated vesicularity of
1313 one of the pumice fragments.

1314

1315 Figure 10: Mean beach-ridge elevation variability along shore-normal Transects B (a), A (b) and
1316 C (c). See Fig. 11a for the location of the individual transects. Notice relatively high beach-ridge
1317 elevations around 800-950 CE for all three transect. This period is known for the occurrence of
1318 multiple prolonged droughts, and has been related to the Classic Maya collapse.

1319

1320 Figure 11: Variability in shore-parallel beach-plain progradation rate (b) and mean elevation (c)
1321 for Phase 2 (1800 BCE - 150 CE) (orange/red) and Phase 3C (1460 - 1965 CE) (green). Dashed
1322 lines represent calculated elevation values for constant 'aeolian' accretion rates. Arrows in panel
1323 (a) indicate the estimated dominant direction of swell driving the formation of the swash
1324 deposits, and the dominant wind direction related to aeolian sand transport, responsible for the
1325 formation of an aeolian cap on top of the swash-built beach ridges.

1326

1327 Figure 12: Periodicities of beach-ridge formation for the Usumacinta-Grijalva (Us-Gr) system
1328 compared with reported or estimated values for other large beach-ridge systems: Rockingham
1329 Bay (Forsyth et al., 2010), Beachmere (Brooke et al., 2008b), Moruya (Oliver et al., 2015),
1330 Guichen Bay (Murray Wallace et al., 2002; Bristow and Pucillo, 2006), Keppel Bay (Brooke et
1331 al., 2008a), Shark Bay (Nott, 2011), Cowley beach (Nott et al., 2009), Lake Michigan
1332 (Thompson, 1992), Sint Vincent Island (Lopez and Rink, 2008; Rink and Lopez, 2010), Jerup
1333 (Nielsen et al., 2006), Nayarit (Curry et al., 1969) and Rio Grande do Sul (Milana et al., in
1334 press).

1335

1336 Table 1. General characteristics for the watersheds of the main rivers draining towards the
1337 Usumacinta-Grijalva delta.

1338

1339 Table 2: General characteristics of the beach-ridge plain along the shore-normal transects as
1340 indicated in figure 2A.



1341

1342 **Appendix A**

1343

1344 Table A1: AMS ¹⁴C-dated samples.

1345

1346 Table A2: OSL-dated samples

1347

1348 Table A3: Major-element composition (mean and standard deviation) of volcanic glass and
1349 pumice fragments recovered from the beach-ridge sediments along Transect A. Oxide
1350 concentrations are normalized to 100% on a volatile-free basis. All iron is taken as FeO. The
1351 major-element composition of volcanic glass shards from Tierra Blanca III were generously
1352 provided by Hector V. Cabadas-Báez (Cabadas-Báez et al., 2017).

1353

1354 **Appendix B**

1355

1356 Figure B1: Variability in grain-size distribution of sand samples along Transect A at 0.04-14.5
1357 km from the current coastline. Vfs = very fine sand; fs = fine sand; ms = medium sand; cs =
1358 coarse sand. Grain-size distributions of representative surficial samples from the current beach
1359 profile (Fig. 7c) are indicated for comparison.

1360

1361 Figure B2: Age-distance scenarios for Transect B2, assuming a constant aeolian accretion rate in
1362 a shore-normal direction. The combined calibrated ages for OSL and AMS samples 440 and
1363 433/336 (154 +/-65 and 1720 +/-65 BCE), calculated with Oxcal 4.2 (Bronk Ramsey, 2009)
1364 using the IntCal13 calibration curve (Reimer et al., 2013), are used as model boundaries.
1365 Indicated are five long-range (red) and five short-range (blue) scenarios for Transect B2-1 – B2-
1366 5. The calibrated 1 sigma age range for a P_sequence model solely based on OSL ages
1367 (excluding sample 437) is indicated in grey.

1368

1369

1370

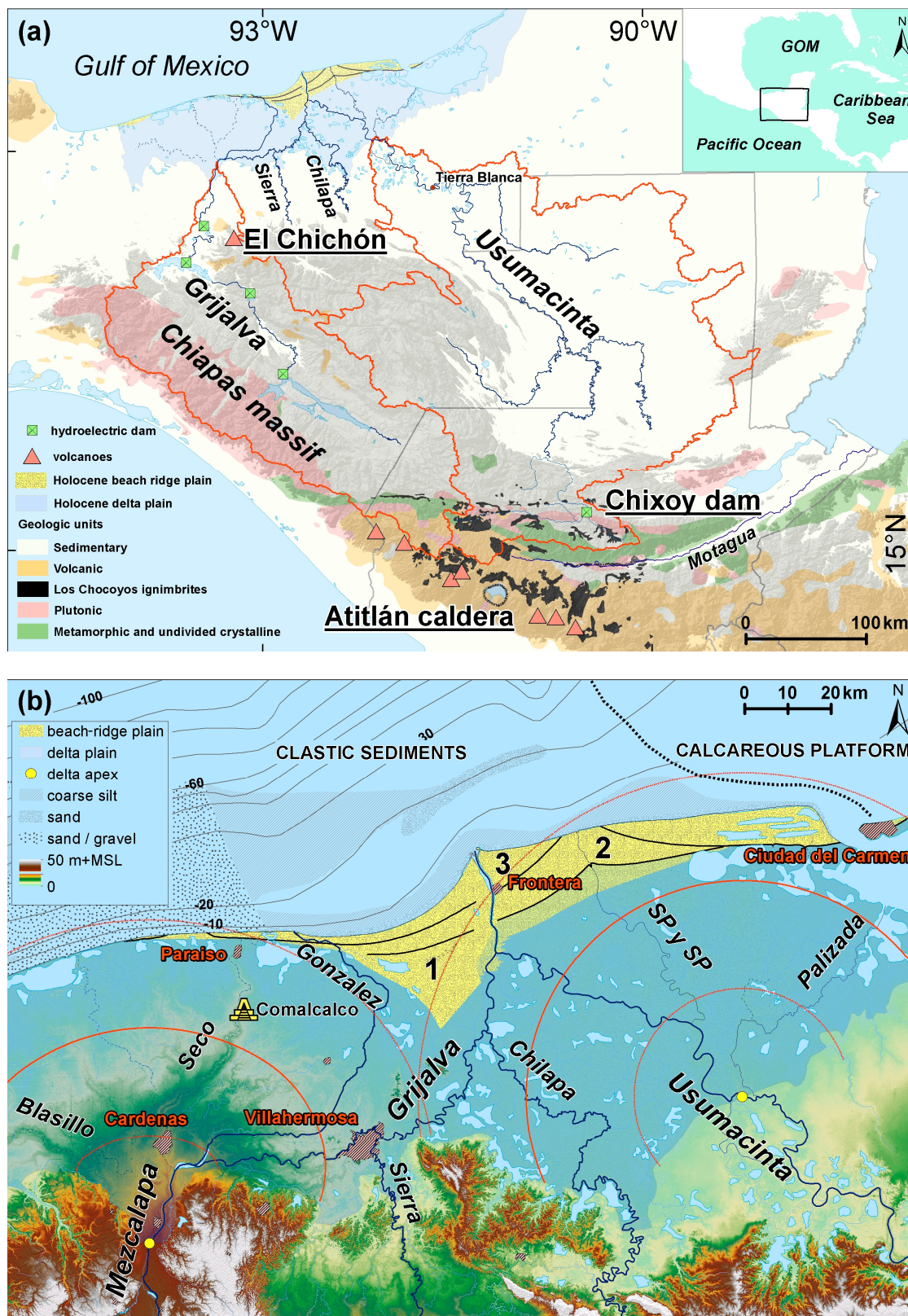


Figure 1

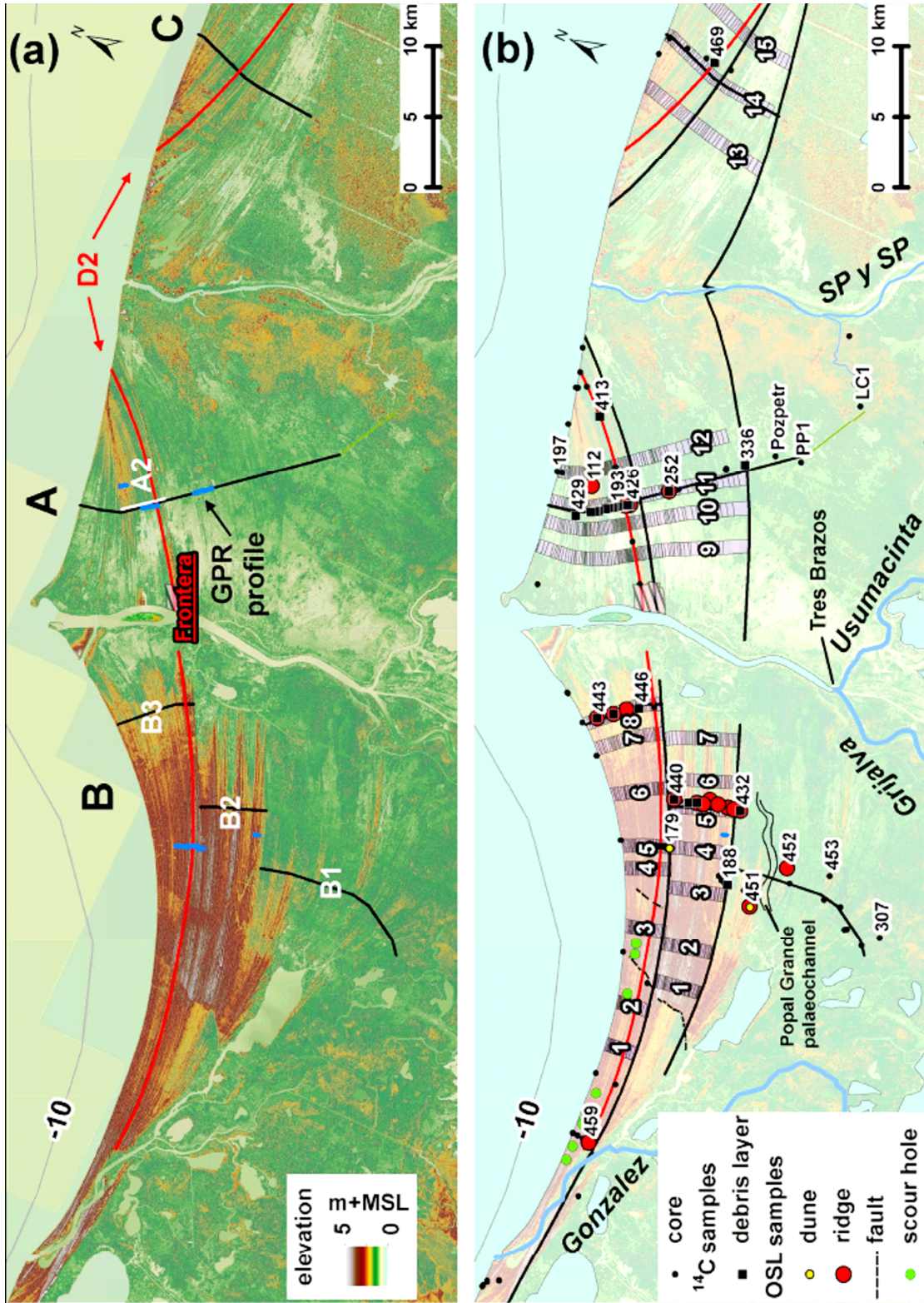


Figure 2

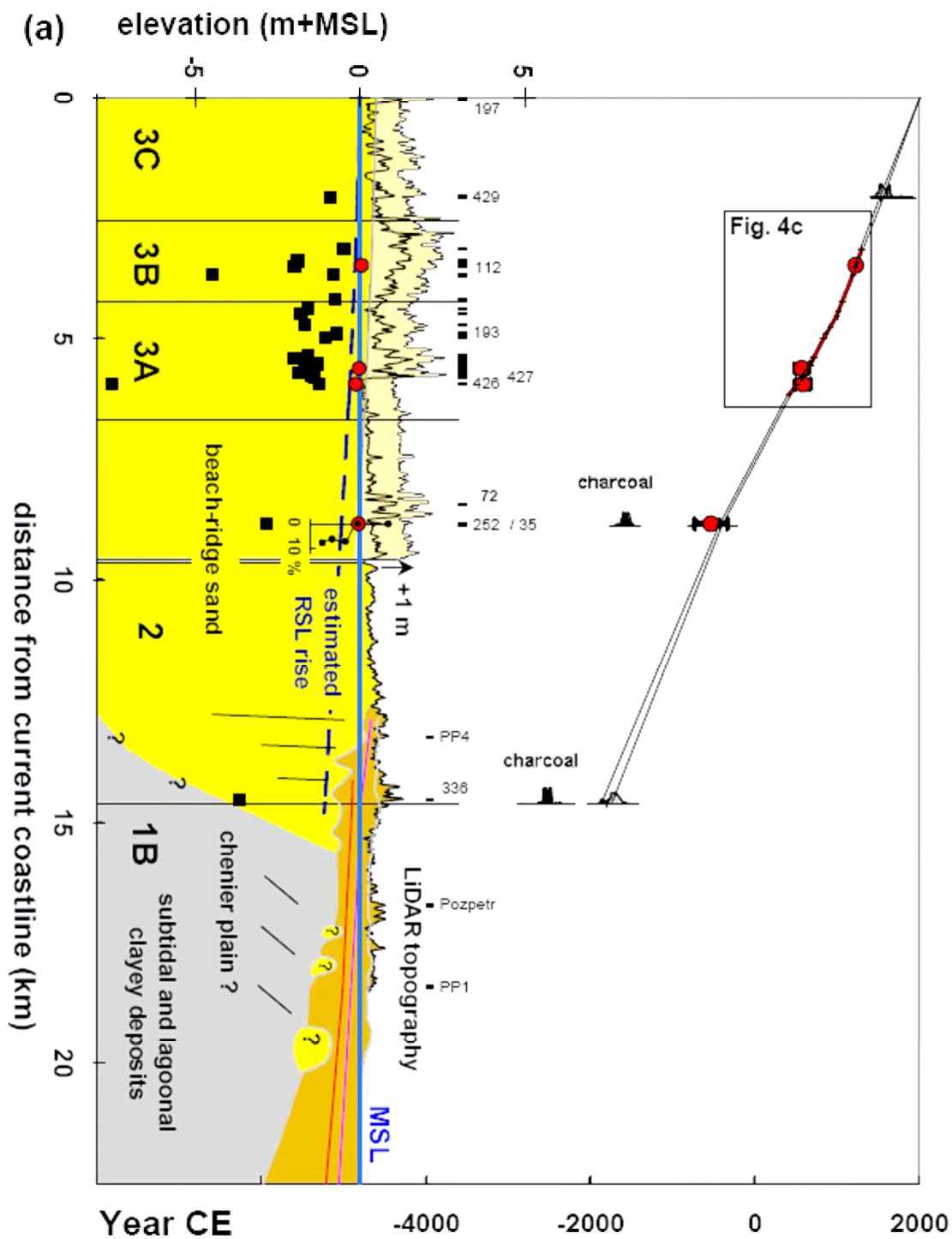


Figure 3a

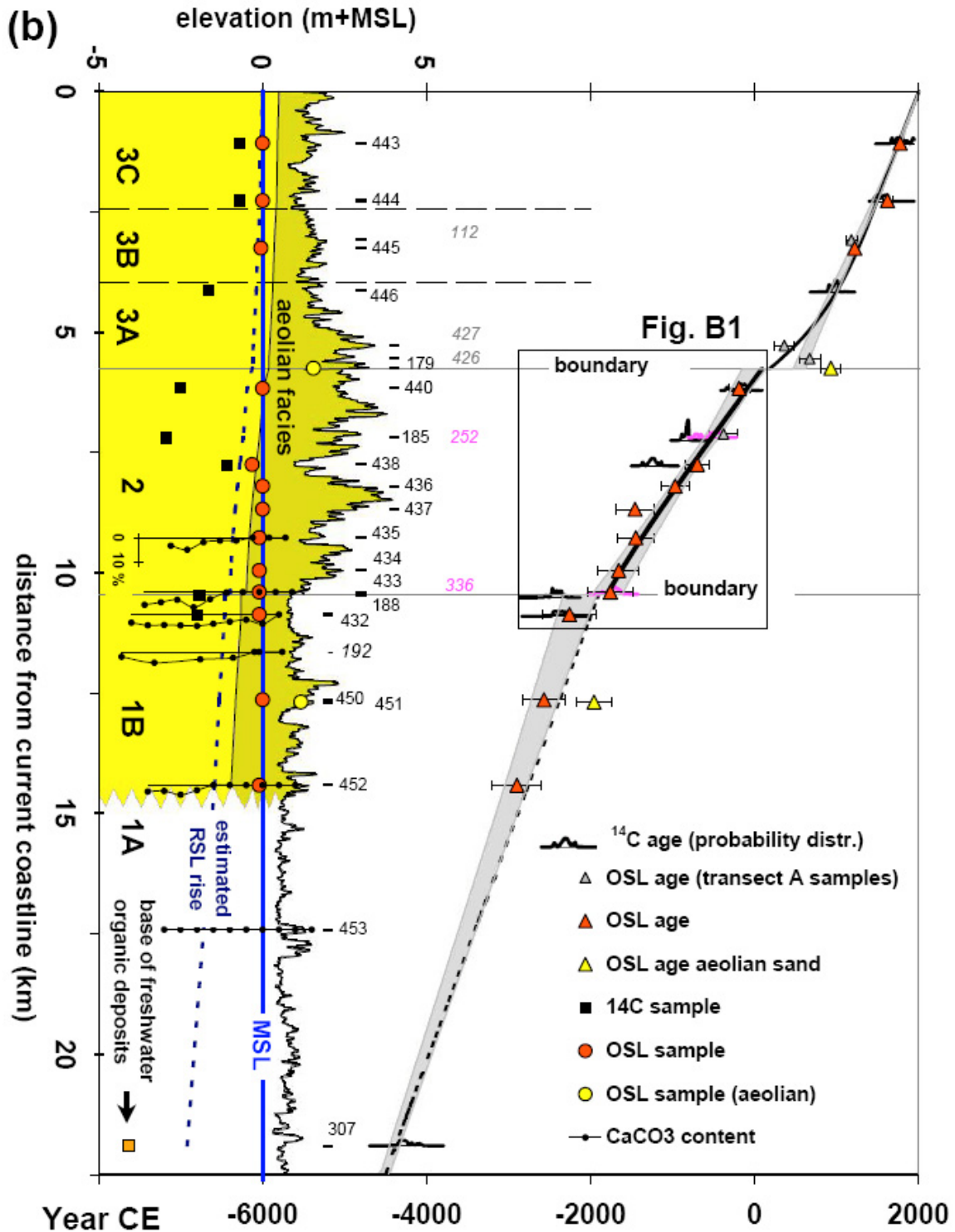


Figure 3b

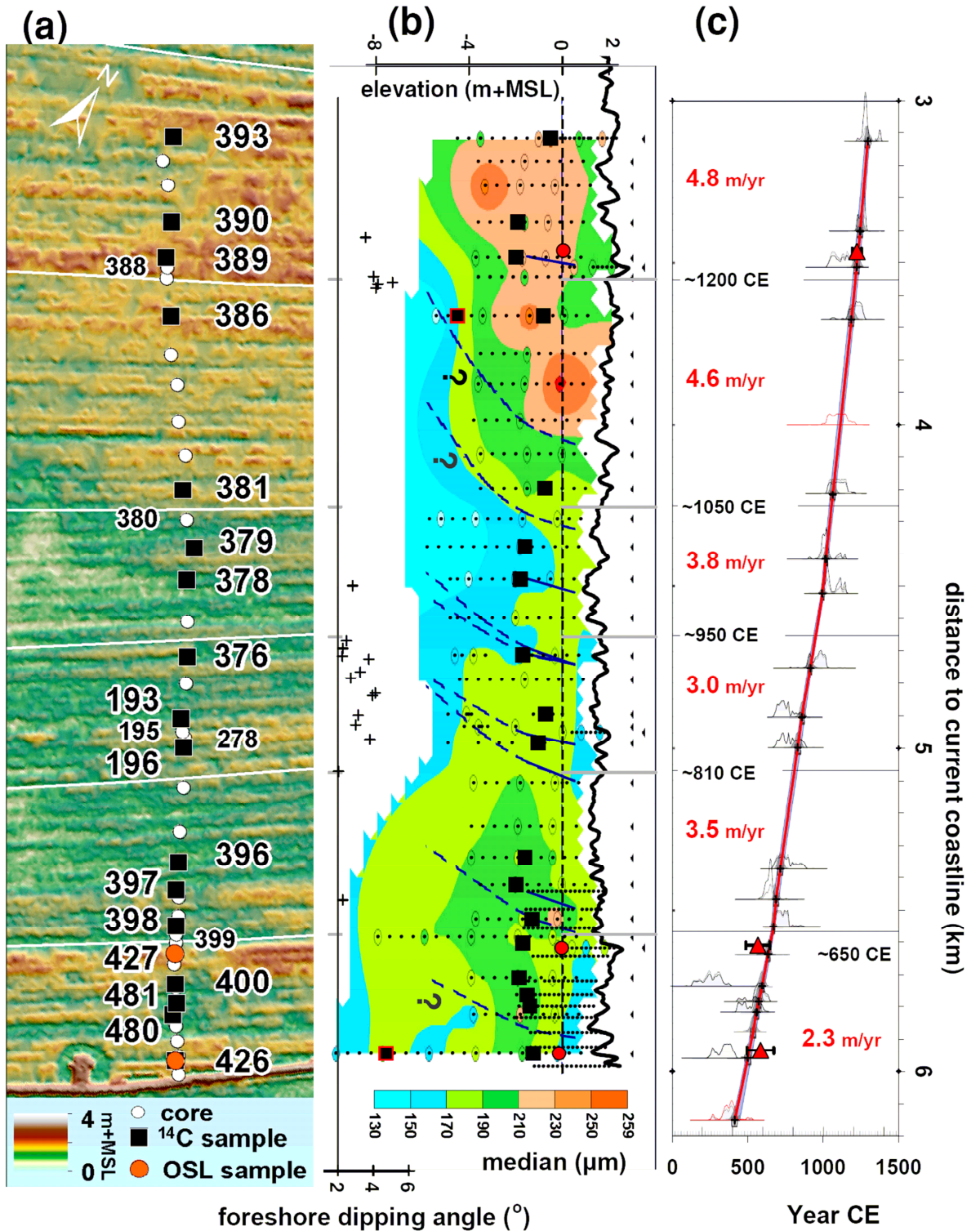


Figure 4.

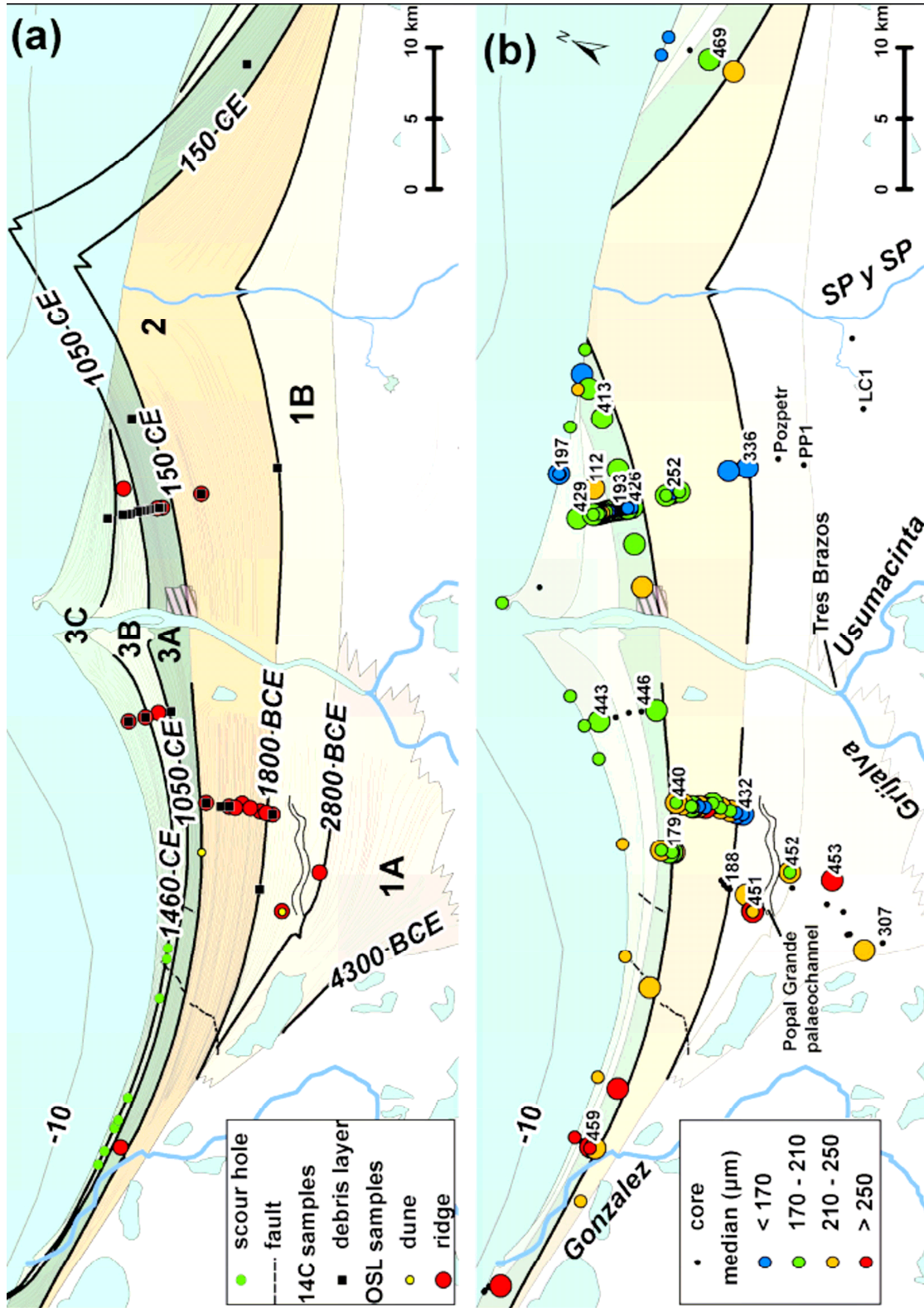


Figure 5

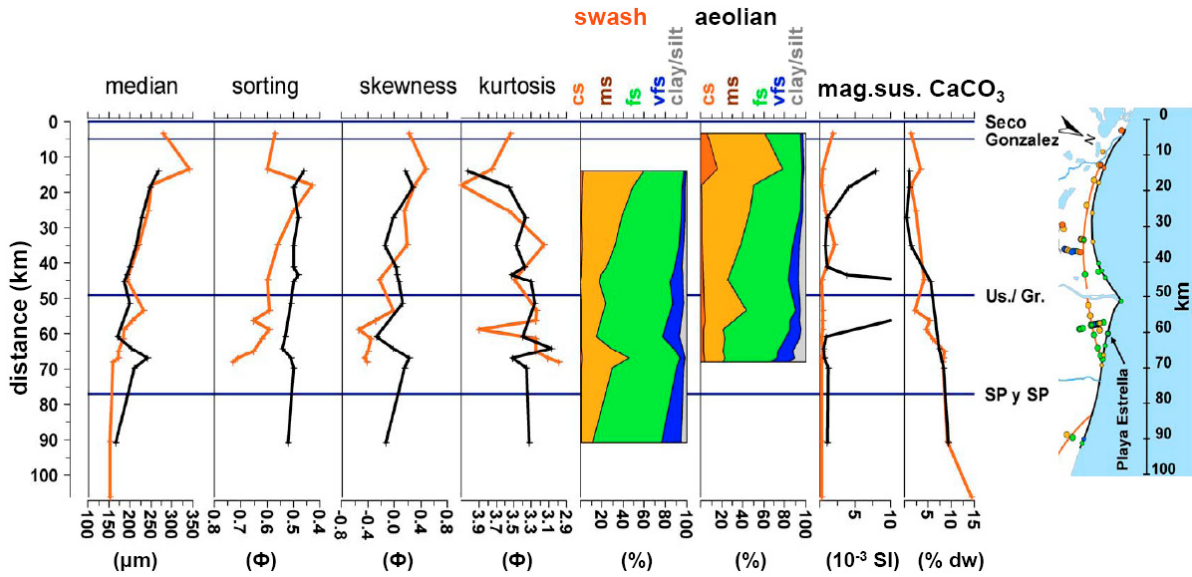


Figure 6.

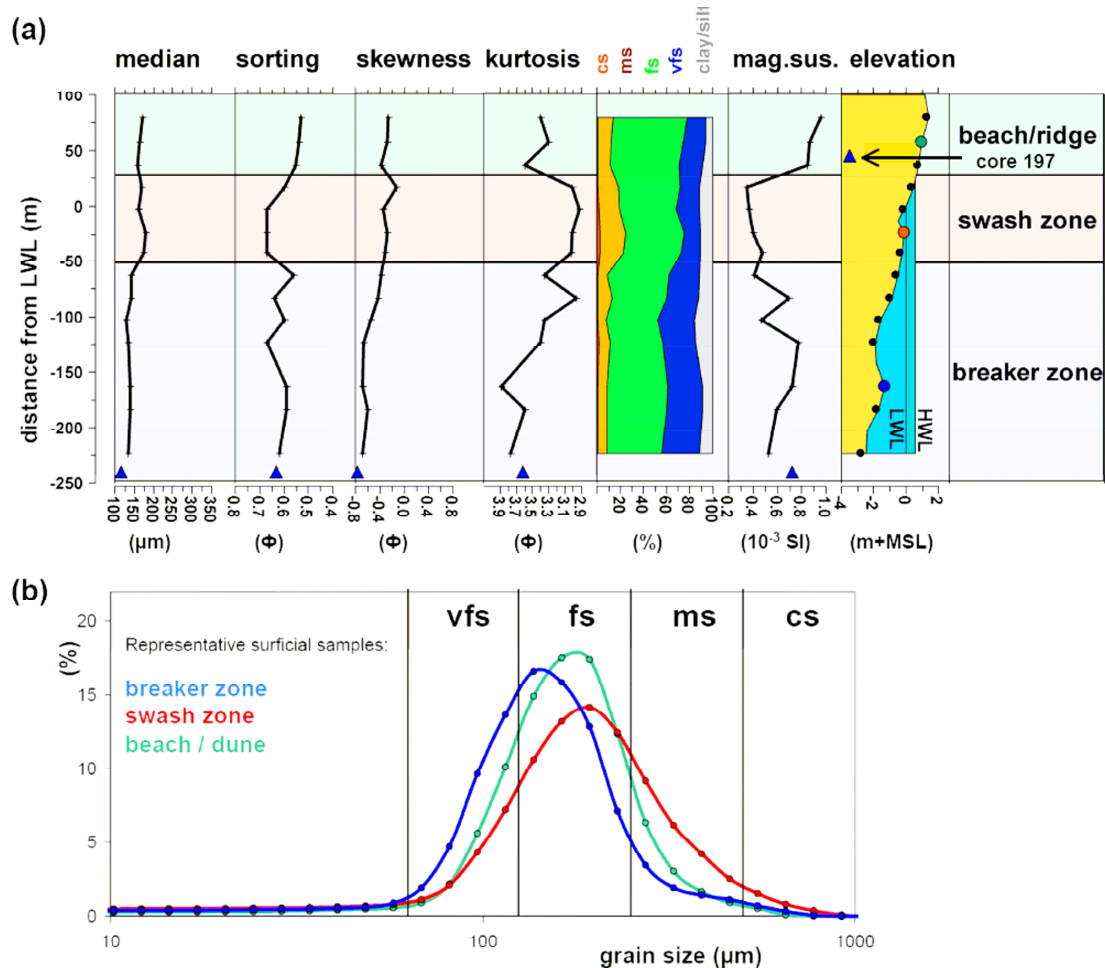


Figure 7

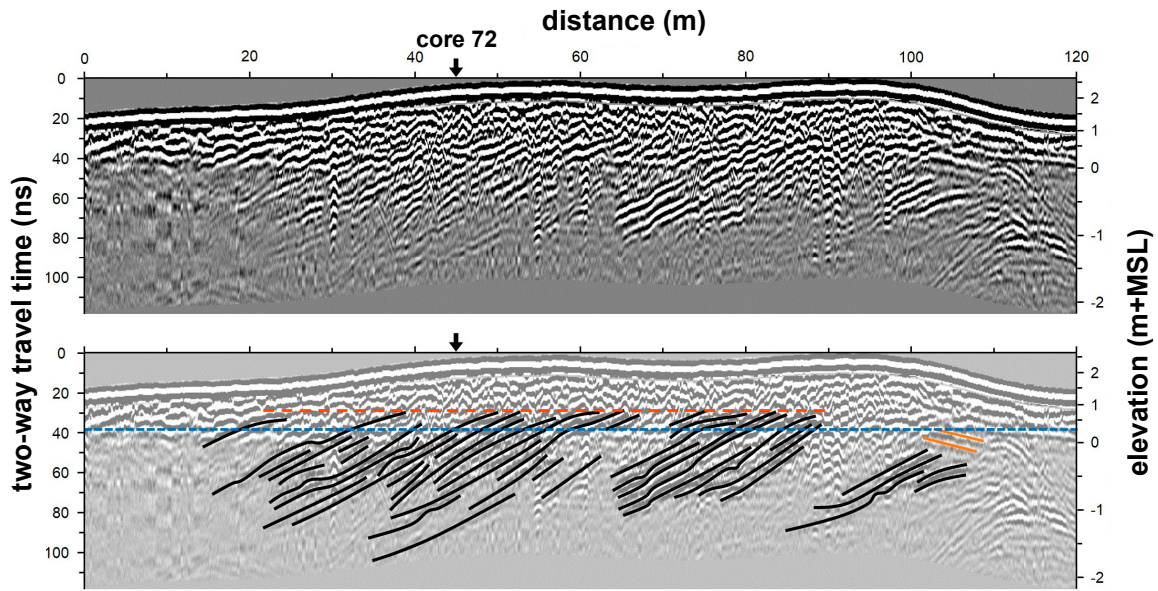


Figure 8

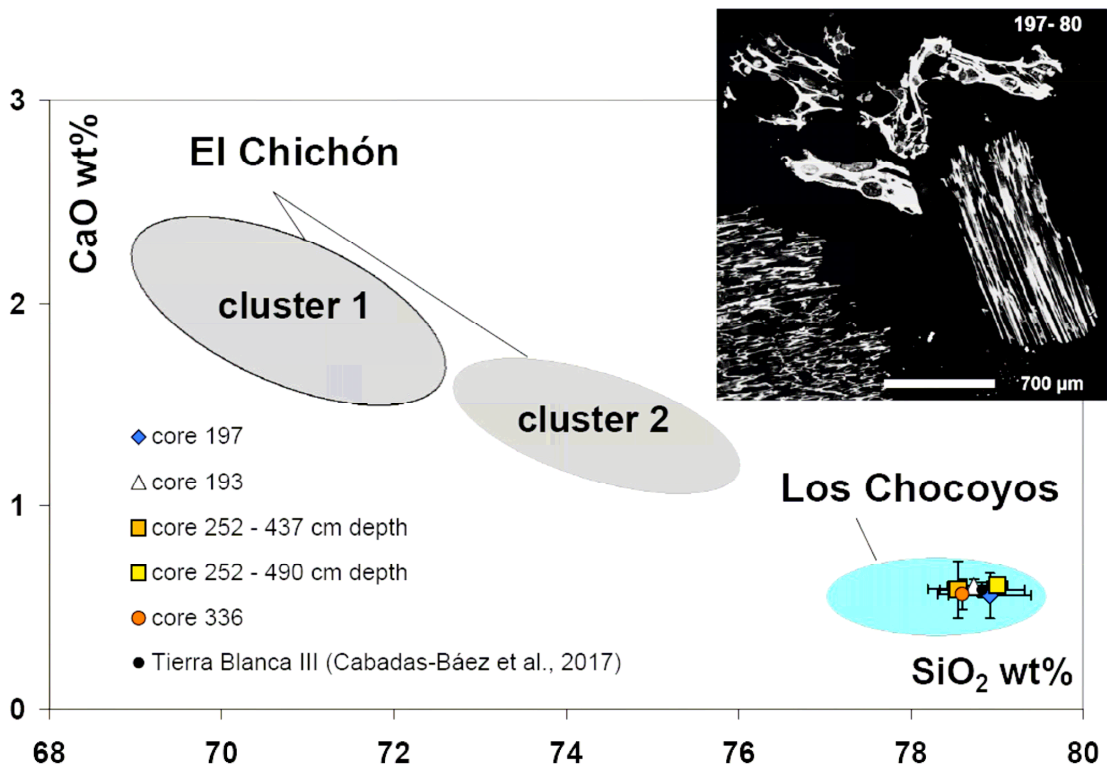


Figure 9.

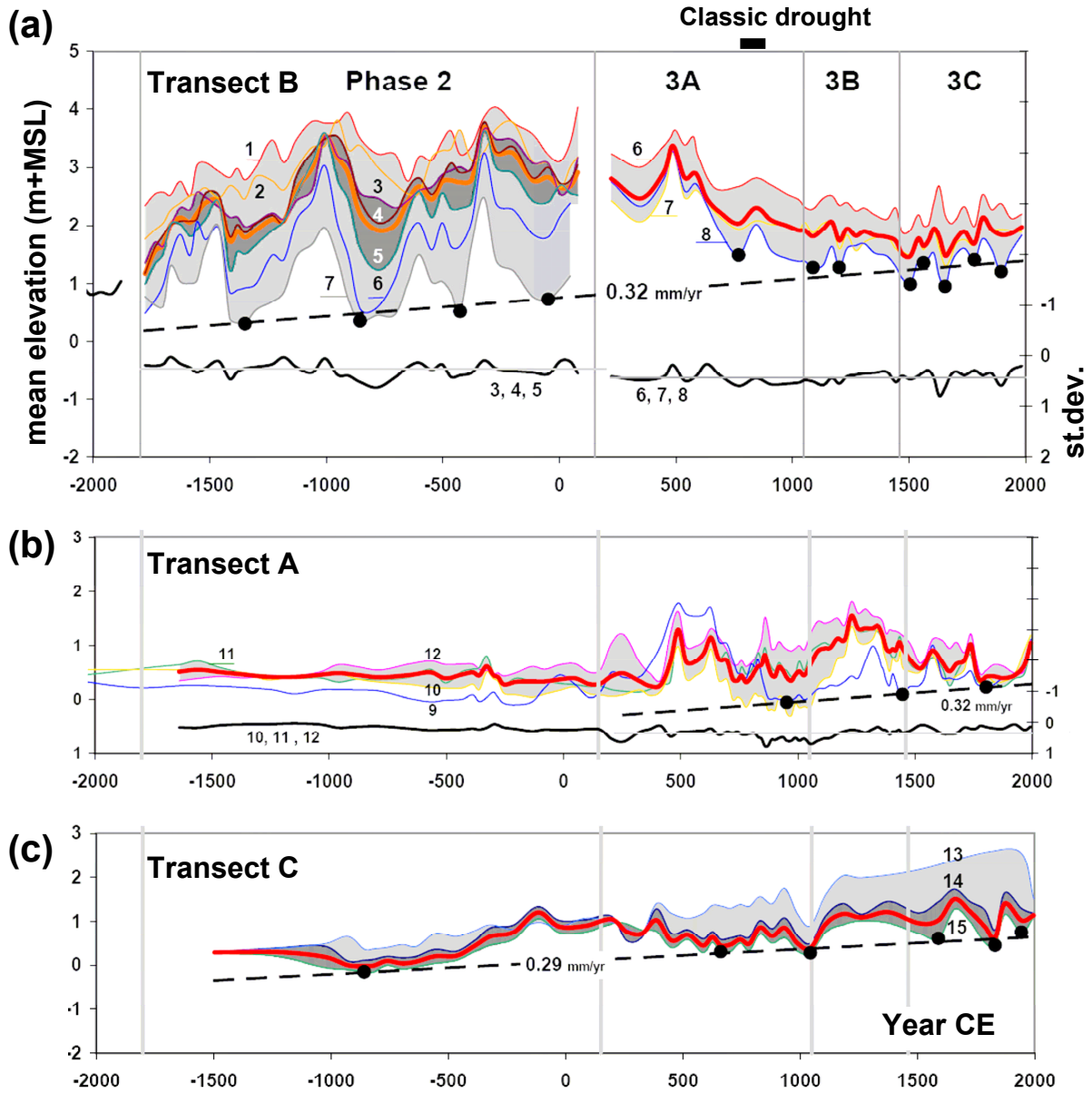


Figure 10.

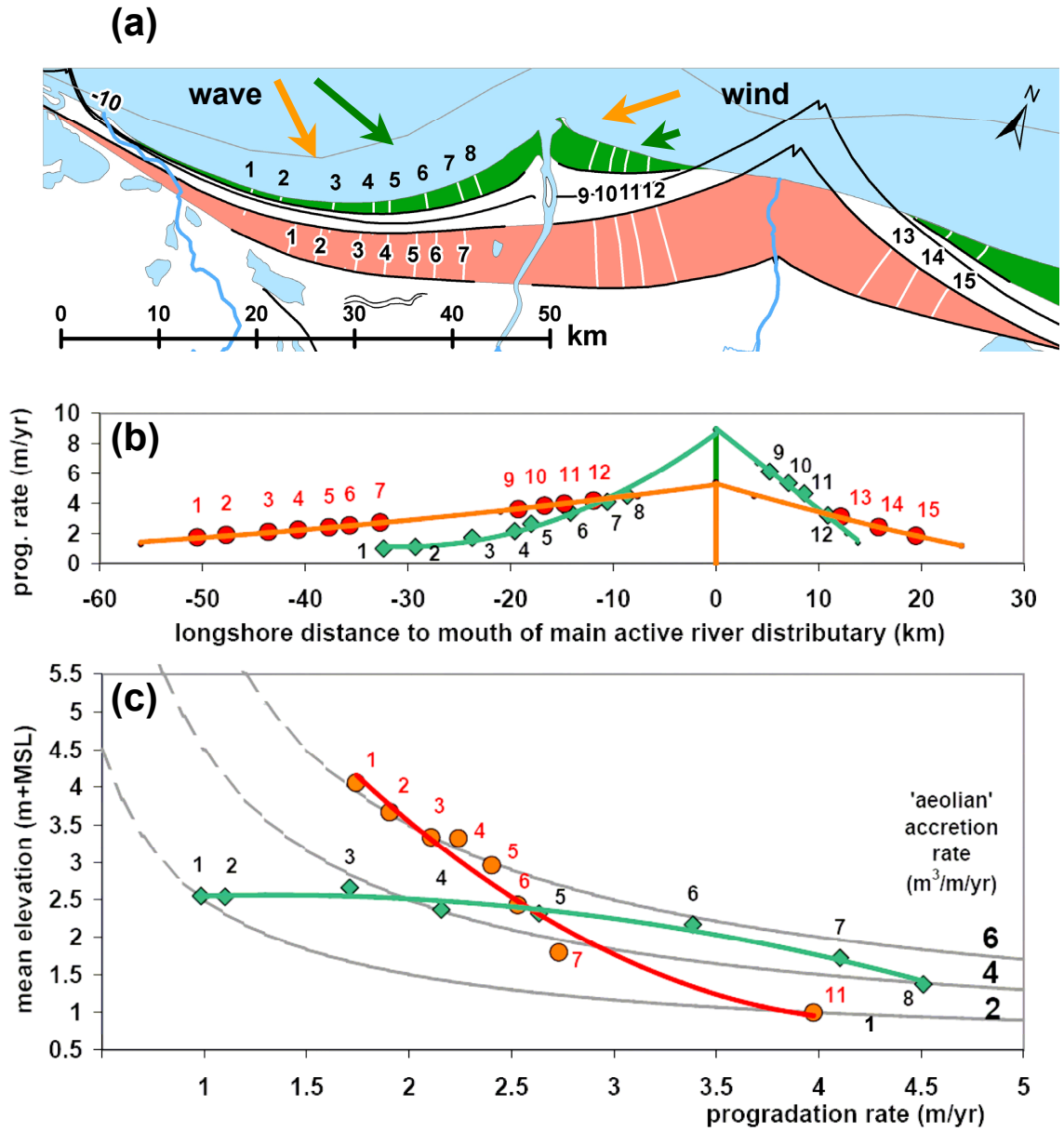


Figure 11.

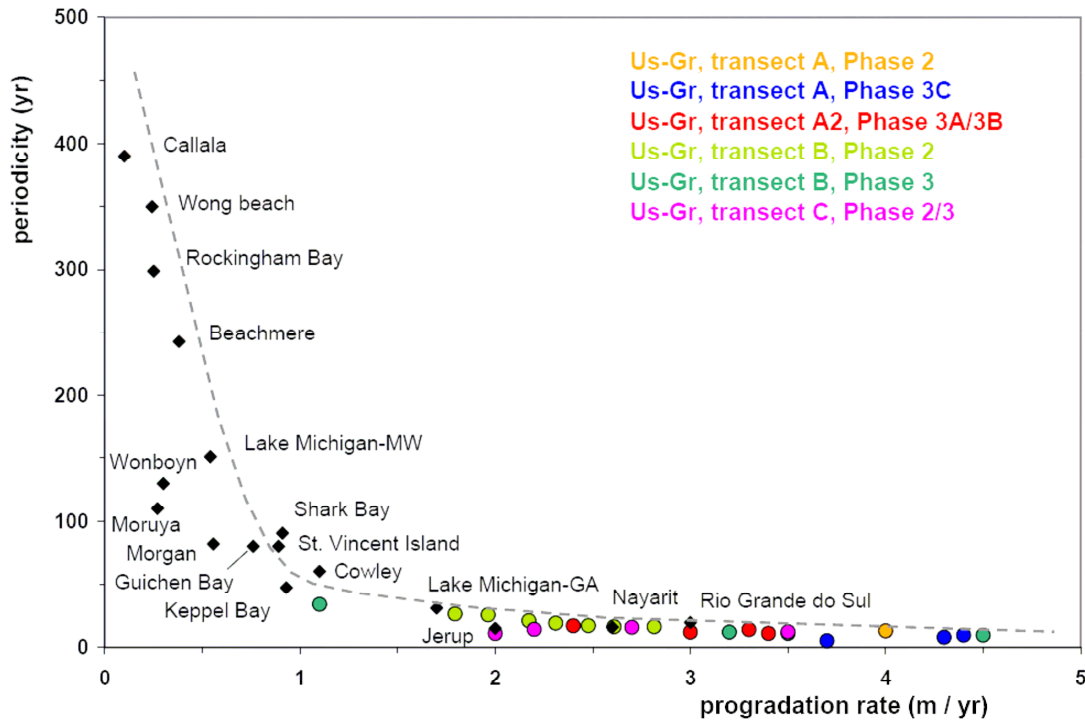


Figure 12

Table 1.

catchment	areal extent		average annual precipitation (mm/yr) ¹	average annual discharge (m ³ /s) ²	excess rainfall (%)
	(km ²)	(%)			
Usumacinta	70714	58	2150	2000	41
Grijalva	37471	31	1500	750	42
Sierra/Chilapa system	12840	11	2550	600	58

1. mean value for the watershed, calculated over the period 1950-2000 (WorldClim version 1.4 (release 3); Hijmans et al., 2005)
2. estimated valued based on measured discharges at the different hydrological stations (Banco Nacional de Datos de Aguas Superficiales, consulted in June 2016)

Table 2.

phase	time range Year CE	transect	distance (km)	duration (yr)	mean elevation (m+MSL)	number of ridges	mean		total beach plain accretion (m ³ /m/yr) ¹	mean aeolian accretion	
							periodicity (yr)	progradation rate (m/yr)		(m ³ /m/yr)	(%)
3c	1460 - 2007	A	2.5	547	1.5 ²	58	9.4	4.5	36 - 54	4.3	8 - 12
	1460 - 2007	B3	2.5	547	1.41	57	9.6	4.5	36 - 54	4	7 - 11
	1460 - 2007	C	1.1	547	1.37	50	10.9	2.0	16 - 24	2.6	11 - 16
3b	1050 - 1460	A	1.6	410	2.1 ²	59	6.9	4.0	32 - 48	6.1	13 - 19
	1050 - 1460	B3	1.4	410	1.49	37	11.1	3.5	28 - 42	3.6	9 - 13
	1050 - 1460	C	0.9	410	1.31	29	14.1	2.2	17 - 26	2.7	10 - 16
3a	150 - 1050	A	2.4	900	1.55 ²	61	14.8	2.7	21 - 32	2.7	8 - 13
	150 - 1050	B3	1.9	900	2.03	47	19.1	2.1	17 - 25	2.9	12 - 17
	150 - 1050	C	3.1	900	0.78	74	12.2	3.5	28 - 42	2.6	6 - 9
2	-1800 - 150	A	7.8	1950	1.44 ²	150	13.0	4.0	32 - 48	3.6	8 - 11
	-1800 - 150	B2	4.7	1950	2.21	120	16.3	2.4	19 - 29	5.8	20 - 30
	-1400 - 150	C	4.3	1550	0.47	98	15.8	2.7	22 - 33	1.2	4 - 5
1	4300 - 1900	B1	11.1	2400	0.82	154	15.6	4.6	-	-	-

1. assuming an average thickness for the beach ridge deposits of 8 - 12 m
2. 1 m was added to the LIDAR-elevation data from 2008



Appendix A

Table A1

sample	dist. along transect (m)	GrA	Age BP	sigma	extracted fraction	d ¹³ C (‰)	C (%)	
TRANSECT A								
debris layers within beach ridge sands								
	429-250L	2110	58037	300	35	leaf fragments	-27.39	49.78
A2 ¹⁾	393-300L	3120	58032	715	35	leaf fragments	-30.25	45.26
A2	390-330L	3375	59436	755	30	leaf fragments	-29.45	49.48
A2	389-330L	3485	58031	900	40	leaf fragments	-30.48	52.21
A2	386-240L	3665	59755	820	40	leaf fragments	-31.97	51.93
A2	386-610L	3665	59751	940	50	leaf fragments	-30.52	49.28
A2	381-225L	4195	59753	935	35	leaf fragments	-31.12	55.98
A2	379-280L	4375	58030	1015	35	leaf fragments	-28.29	48.16
A2	378-280L	4475	59435	990	30	leaf fragments	-28.95	52.84
A2	376-290L	4710	59752	1075	40	leaf fragments	-28.29	42.98
A2	193-171L	4890	55022	1250	30	leaf fragments	-30.05	61.50
A2	196-204L	4978	55023	1235	30	leaf fragments	-30.94	61.50
A2	396-270L	5330	59757	1255	40	leaf fragments	-30.94	51.96
A2	397-350L	5415	58033	1390	35	leaf fragments	-30.06	54.93
A2	398-260S	5520	59437	1270	30	squash seed	-29.45	49.48
A2	413-270L	5595	59438	1415	30	leaf fragments	-28.72	50.93
A2	400-295L	5700	59694	1775	40	leaf fragments	-30.31	45.30
A2	481-290L	5755	60873	1490	35	leaf fragments	-29.65	51.11
A2	480-290L	5790	60871	1525	35	leaf fragments	-29.74	51.38
A2	426-885L	5935	58035	1665	35	leaf fragments	-29.92	45.92
A2	426-255L	5935	58034	1690	40	leaf fragments	-29.75	52.56
	252-485L	8642	55021	2420	35	leaf fragments	-31.42	55.10
	252-485C	8642	55024	3290	30	charcoal	-24.66	73.70
	336-368L	14222	54940	3410	45	leaf fragments	-29.7	38.70
	336-368C	14222	55025	3990	35	charcoal	-25.02	68.20
base of freshwater peat								
	Pozpetr.-78-82 ²⁾		UtC-11090	2055	59	charcoal/wood	-28.2	
	PP1-169-170 ¹⁾		53751	3220	40	charred plant fragments	-21.55	53.40
base of mangrove peat								
	LC1-315-320		55026	5030	35	charred plant fragments	-23.78	79.20
TRANSECT B								
debris layers within beach ridge sands								
	443-230L	1075	58041	165	35	leaf fragments	-28.11	50.18
	444-150L	2270	58042	350	35	leaf fragments	-28.64	49.99
	446-275L	4134	58043	1060	40	leaf fragments	-29.53	52.03
	440-350L	6168	58040	2125	40	leaf fragments	-29.82	50.59
	185-471L	7195	55029	2665	35	leaf fragments	-28.61	42.30
	438-170L	7752	58039	3005	35	leaf fragments	-29.64	52.59
	188-310L	10468	55020	3930	35	leaf fragments	-30.33	51.60
	432-300L	10866	58144	3880	40	leaf fragments	-30.65	51.86
base of freshwater peat								
	307-405-410S	21901	64320	5420	70	Asteraceae seeds	-28.08	
TRANSECT C								
	469-160L		58044	1210	35	leaf fragments	-29.63	49.70
	469-325L		58048	1360	35	leaf fragments	-29.51	46.92

1) Nooren et al., 2017

2) Nooren et al., 2009



Table A2

sample	NCL code	Lat. (°)	Long. (°)	comp. dist. ¹⁾ (m)	depth (m)	elev. (m+MSL)	water content meas. used (% dw)	organic content (% dw)	U ²³⁸ (Bq/kg)	Th ²³² (Bq/kg)	K ⁴⁰ (Bq/kg)	unatten. doser. β (Gy/ka)	cosmic radiation (Gy/ka)	burial dose ²⁾ (Gy)	over-dispersion (%)	dose rate (Gy/ka)	age (Year CE)	validity															
Transect A																																	
112	NCL-4112227	18.595	-92.594	3085	1.9	0	16.9	25 5	30.43	0.41	38.16	0.96	429	10	1.13	0.07	0.80	0.04	0.16	0.01	1.75	0.12	26	11	2.10	0.09	0.83	0.07	1182	70	Likely OK		
427	NCL-1114072	18.570	-92.596	5280	2.3	0	27.7	25 5	1.26	0.13	13.67	0.17	14.71	0.37	724	15	1.39	0.09	0.65	0.03	0.15	0.01	3.6	0.2	30	4	2.20	0.1	1.65	0.12	363	120	Questionable
426	NCL-4213072	18.568	-92.595	5550	1.3	0	33.1	25 5	0.92	0.09	15.82	0.21	17.92	0.47	750	15	1.48	0.10	0.72	0.04	0.18	0.01	3.2	0.3	21	15	2.39	0.1	1.34	0.13	673	130	Likely OK
252	NCL-4112229	18.549	-92.575	7113	1.9	0	32.8	25 5	0.72	0.07	19.51	0.46	20.34	1.22	632	16	1.33	0.09	0.72	0.04	0.16	0.01	5.3	0.3	26	5	2.22	0.1	2.39	0.17	-378	170	Likely OK
Transect B																																	
443	NCL-4213078	18.530	-92.733	1075	1.6	0	25.9	25 5	0.87	0.09	20.50	0.32	23.05	0.76	577	13	1.25	0.08	0.71	0.04	0.16	0.01	0.5	0.04	20	8	2.13	0.09	0.24	0.02	1773	20	Likely OK
444	NCL-1114071	18.522	-92.726	2270	0.8	0	27.0	25 5	0.85	0.09	19.84	0.31	19.73	0.67	635	14	1.33	0.09	0.71	0.04	0.19	0.01	0.86 ³⁾	0.12	69	18	2.24	0.1	0.39	0.06	1623	60	Likely OK
445	NCL-4213079	18.515	-92.719	3255	1.05	-0.05	25.0	25 5	0.84	0.08	14.83	0.27	15.26	0.68	725	15	1.41	0.09	0.67	0.04	0.18	0.01	1.79	0.08	7	6	2.28	0.1	0.79	0.05	1223	50	OK
179	NCL-4112228	18.452	-92.793	5750	0.55	1.55	4.7	5 3	1.78	0.18	18.87	0.30	23.12	1.58	612	13	1.60	0.09	0.86	0.05	0.20	0.01	2.9	0.3	33	9	2.66	0.1	1.08	0.12	932	120	Questionable
440	NCL-4213077	18.463	-92.761	6168	1	0	23.2	25 5	0.77	0.08	17.61	0.22	19.95	0.49	624	13	1.29	0.08	0.69	0.04	0.19	0.01	4.8	0.2	17	3	2.17	0.09	2.20	0.13	-187	130	OK
438	NCL-4213076	18.449	-92.757	7752	0.92	-0.32	26.2	25 5	0.52	0.05	16.13	0.28	19.16	0.67	627	13	1.30	0.08	0.69	0.04	0.19	0.01	5.9	0.2	10	4	2.18	0.09	2.71	0.15	-697	150	OK
436	NCL-1114073	18.445	-92.756	8199	2.2	0	24.8	25 5	0.87	0.09	15.72	0.23	18.32	0.53	643	13	1.30	0.08	0.68	0.04	0.15	0.01	5.4	0.2	12	3	2.14	0.09	2.98	0.17	-967	170	OK
437	NCL-4213075	18.442	-92.751	8678	1.5	0	25.9	25 5	1.00	0.10	18.22	0.30	21.42	0.74	661	14	1.36	0.09	0.72	0.04	0.17	0.01	7.8	0.4	18	6	2.26	0.1	3.47	0.23	-1457	230	OK
435	NCL-1114074	18.436	-92.751	9272	1.3	-0.1	25.2	25 5	0.93	0.09	18.03	0.28	20.24	0.66	679	14	1.36	0.09	0.69	0.04	0.18	0.01	7.8	0.4	16	5	2.25	0.1	3.46	0.23	-1447	230	OK
434	NCL-4213074	18.430	-92.751	9953	2.7	-0.1	25.8	25 5	1.05	0.11	14.56	0.25	16.65	0.68	658	14	1.31	0.09	0.66	0.04	0.14	0.01	7.8	0.4	23	4	2.13	0.09	3.67	0.25	-1657	250	Likely OK
433	NCL-1114075	18.426	-92.750	10398	1.5	-0.1	26.1	25 5	0.68	0.07	18.86	0.23	21.46	0.50	632	13	1.32	0.09	0.71	0.04	0.17	0.01	8.3	0.5	22	4	2.20	0.09	3.77	0.28	-1757	280	Likely OK
432	NCL-4213073	18.422	-92.749	10866	1.1	-0.1	25.1	25 5	0.25	0.03	14.78	0.26	16.49	0.66	594	13	1.21	0.08	0.63	0.03	0.18	0.01	8.7	0.5	23	4	2.03	0.09	4.27	0.33	-2257	330	Likely OK
450	NCL-4213080	18.390	-92.805	12637	1.05	0	20.9	25 5	0.58	0.06	13.06	0.24	15.49	0.61	529	12	1.08	0.07	0.56	0.03	0.18	0.01	8.4	0.3	12	3	1.83	0.08	4.58	0.26	-2567	260	OK
451	NCL-4213081	18.390	-92.806	12684	1.48	1.17	3.1	5 3	0.86	0.09	12.18	0.17	13.66	0.35	566	12	1.37	0.08	0.66	0.03	0.18	0.01	8.8	0.3	15	2	2.23	0.08	3.97	0.21	-1957	210	OK
452	NCL-1114076	18.379	-92.771	14412	1.6	-0.1	24.5	25 5	0.63	0.06	14.69	0.17	16.62	0.33	595	12	1.21	0.08	0.62	0.03	0.16	0.01	9.8	0.4	22	3	2.00	0.08	4.91	0.3	-2897	300	Likely OK
459	NCL-4213082	18.420	-92.994		0.7	-0.1	22.0	25 5	0.58	0.06	14.64	0.27	18.95	0.70	540	12	1.13	0.07	0.61	0.03	0.19	0.01	2.73	0.13	11	3	1.94	0.08	1.41	0.09	603	90	OK

1) composite distance from current coastline (m), projected along transect B (Fig. 3b)
 2) the bootstrapped version of the Central Age Model (Cunningham and Wallinga, 2012) was applied to determine the burial dose of the samples.
 3) for this sample the bootstrapped version of the Minimum Age Model (Cunningham and Wallinga, 2012) was applied to determine the burial dose. As over-dispersion input value (sigma_b) 18 ± 6% was used.
 alpha dose rate of 0.010 ± 0.005 assumed for all samples



Table A3

core	depth	n	SiO ₂	TiO ₂	Al ₂ O ₃	FeO	MnO	MgO	CaO	Na ₂ O	K ₂ O	P ₂ O ₅	S	Cl	total	before
(m)	(m)		(%) ±	(%) ±	(%) ±	(%) ±	(%) ±	(%) ±	(%) ±	(%) ±	(%) ±	(%) ±	(%) ±	(%) ±	(%)	norm.
197	0.8	10	78.87	0.10	12.28	0.56	0.08	0.09	0.57	3.02	4.27	0.01	0.01	0.12	100	97.34
193 ¹⁾	5	7	78.72	0.10	12.36	0.55	0.06	0.09	0.60	3.19	4.19	0.01	0.01	0.11	100	98.09
252	4.4	14	78.52	0.11	12.24	0.69	0.06	0.09	0.60	3.38	4.18	0.01	0.01	0.12	100	98.07
252	4.9	10	79.00	0.10	12.19	0.52	0.06	0.09	0.61	3.10	4.20	0.01	0.02	0.11	100	97.51
336	3.2	13	78.56	0.10	12.15	0.64	0.07	0.08	0.55	3.30	4.39	0.01	0.02	0.12	100	98.41
			0.31	0.01	0.13	0.19	0.03	0.01	0.08	0.14	0.22	0.02	0.02	0.03		0.39
<hr/>																
			SiO ₂	TiO ₂	Al ₂ O ₃	FeO	MnO	MgO	CaO	Na ₂ O	K ₂ O	BaO	NiO	Cr ₂ O ₃		
			(%) ±	(%) ±	(%) ±	(%) ±	(%) ±	(%) ±	(%) ±	(%) ±	(%) ±	(%) ±	(%) ±	(%) ±		
TB III ²⁾		14	78.83	0.10	12.84	0.58	0.07	0.08	0.59	2.72	4.09	0.11	0.01	0.00	100	97.98
			0.49	0.01	0.37	0.05	0.02	0.01	0.04	0.39	0.22	0.04	0.02	0.00		2.57

1. pumice clast of 1.5 cm diameter
2. Tierra Blanca (Cabadas-Báez et al., 2017)



Appendix B

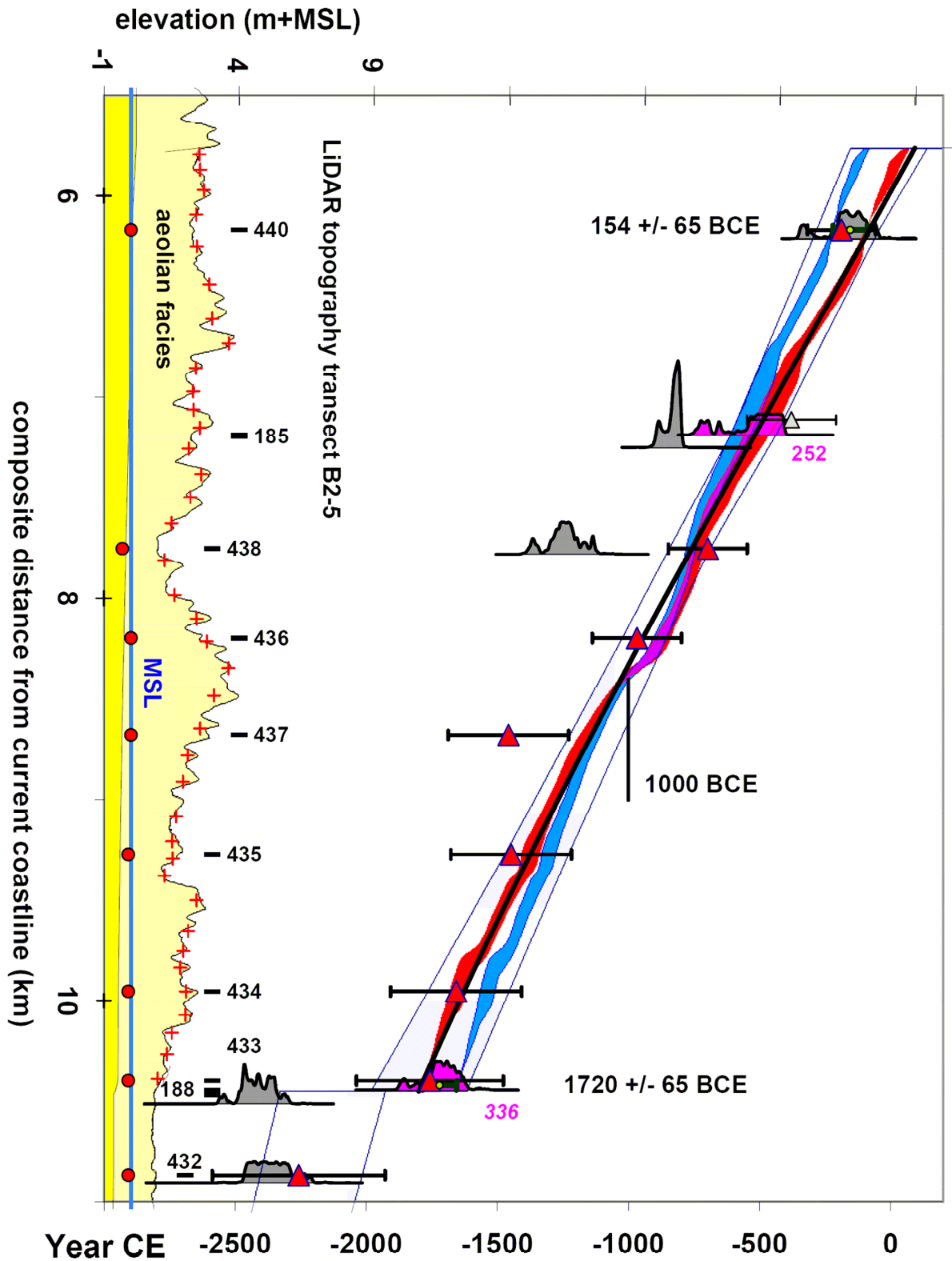


Figure B1

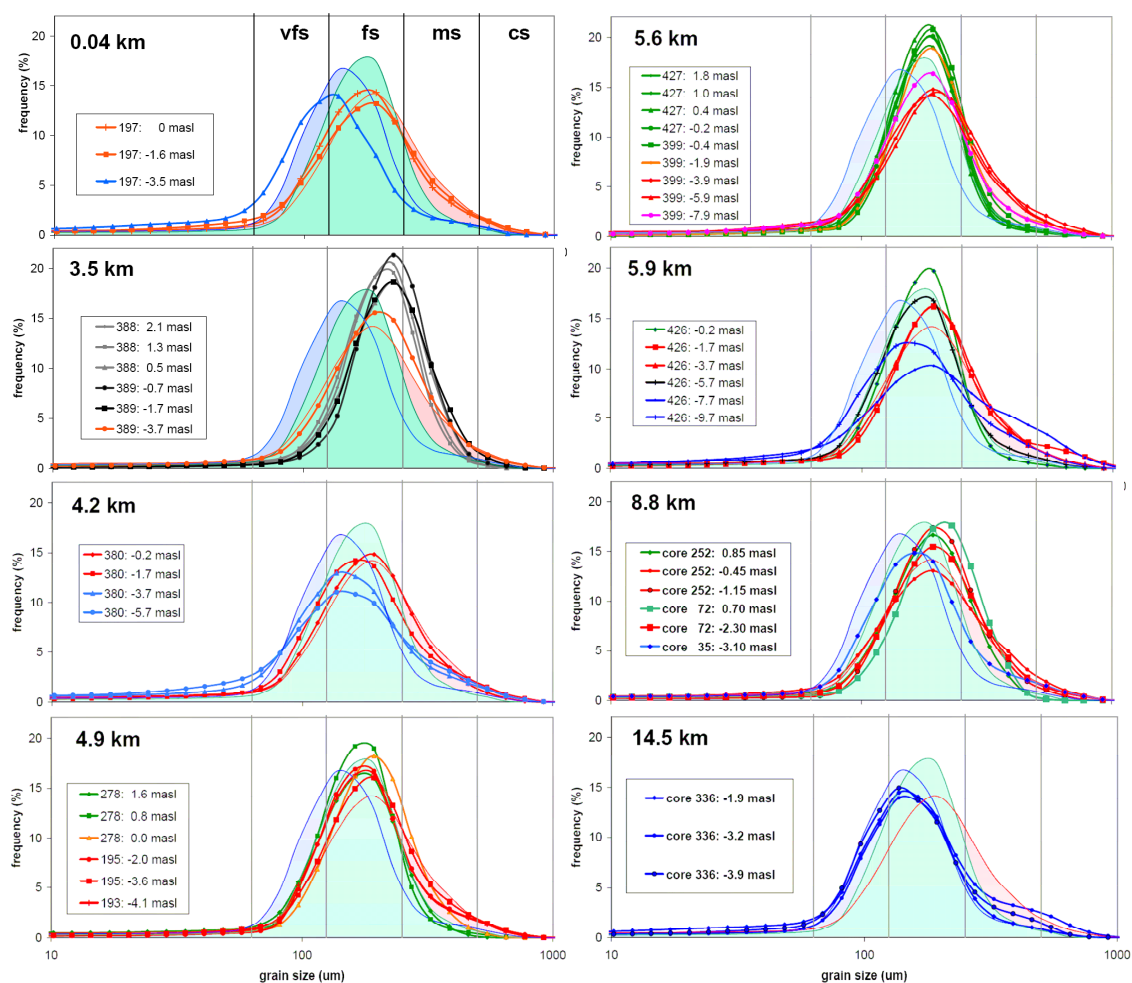


Figure B2